AUTOMATIC ROI SELECTION FOR MULTI-MODAL MEDICAL IMAGES

Chowdhury Mohammad Abid Rahman

BSc Engg. (EEE), RUET

Student No - 1014160008 (P)

A THESIS SUBMITTED FOR THE DEGREE OF

MASTER OF SCIENCE

IN

ELECTRICAL, ELECTRONIC AND COMMUNICATION ENGINEERING

DEPARTMENT OF
ELECTRICAL, ELECTRONIC AND COMMUNICATION ENGINEERING

MILITARY INSTITUTE OF SCIENCE AND TECHNOLOGY
MIRPUR CANTONMENT, DHAKA–1216

2020

APPROVAL CERTIFICATE

The thesis titled "**Automatic RoI Selection for Multi-modal Medical Images**" submitted by Chowdhury Mohammad Abid Rahman, Session: 2014-2015 has been accepted as satisfactory in partial fulfillment of the requirements for the degree of Master of Science in Electrical, Electronic and Communication Engineering on 07 July 2020.

BOARD OF EXAMINERS

1. _____ Chairman
   Lieutenant Colonel Hussain Md. Abu Nyeem, PhD, EME (Supervisor)
   Instructor Class A
   Department of EECE, MIST, Dhaka–1216

2. _____ Member
   Brigadier General A K M Nazrul Islam, PhD (Ex-officio)
   Head of the Department
   Department of EECE, MIST, Dhaka–1216

3. _____ Member
   Air Commodore Md Hossam-E-Haider, PhD (Retd) (Internal)
   Professor
   Department of EECE, MIST, Dhaka–1216

4. _____ Member
   Dr. Satya Prasad Majumder (External)
   Professor
   Department of EEE, BUET, Dhaka–1205

CANDIDATE'S DECLARATION

I hereby declare that this thesis is my original work and it has been written by me in its entirety. I have duly acknowledged all the sources of information which have been used in the thesis.

This thesis has also not been submitted partially or fully for any degree in any university previously.

Signature: _____

(Chowdhury Mohammad Abid Rahman)

Date: 07 July 2020

DEDICATION

To my parents and family

ACKNOWLEDGEMENTS

It is an immense pleasure for me to complete my M.Sc. research work and write-up of this thesis. The completion of this work always reminds me of the continuous support of my supervisor, colleagues, friends, and family. At the end of this research, it is a pleasure to thank everyone.

First and foremost, I would like to express sincere gratitude to my supervisor, Lt Col Hussain Md Abu Nyeem, PhD, EME. I am grateful to him for his continuous support, motivation, enthusiasm, valuable advice, and guidance to complete this thesis work. My supervisor taught me the procedure of conducting research from the very elementary level, and his positive words gave me the fuel to go on my days of frustration. He has also taught me how to work under the pressure of official works. Once again, I thank my supervisor, with whom I feel that I genuinely have been privileged to work.

Moreover, I profoundly thank Lt Col Md Tawfiq Amin, PhD, EME, for his kind coordination and cooperation as the postgraduate course coordinator. I am grateful to my colleagues and friends for making my working at MIST and BMA, more than comfortable and enjoyable. Especially, I express my gratitude to Maj Md Abdul Wahed, Sigs for his cooperation and help to find a solution, technical or otherwise. I would be pleased to extend my sincere thanks to all of my course teachers, Captain Marzuka Ahmed Jumana, Sigs, and staffs of the EECE department, MIST, for their kind support.

I thank each member of my family for being understanding and supportive. I greatly remember my father, late Md. Mashiur Rahman Chowdhury, who would have become highly proud and possibly the happiest person on this earth to see me graduated. My Mother Kabita Khanam has been my biggest support and source of continuous inspiration despite her overwhelming official commitments. I have been more than beholden forever to my wife Rumana Subnom Turin, for her unconditional and endless support to get my stress down and to complete my work with full enthusiasm. I remain thankful to my loving elder sister Dr. Mumtahinah Qudsiah, brother-in-law Dr. A K Parvaz Rinku, and cute niece Opshori. Finally, I would also like to thank Mrs. Luisa Fozila Chowdhury, the spouse of my supervisor, who has always been loving and caring to my family and me.

CHOWDHURY MOHAMMAD ABID RAHMAN

Dhaka, Bangladesh

July 2020

CONTENTS

ABSTRACT

The Region of Interests (RoIs) in Medical Images (MIs) contain specialized form of clinical and biological data important for medical procedures and practices. Their detection with higher accuracy and representation with more efficiency have become two important requirements of many region-based MI processing. However, these requirements are largely overlooked in contemporary literature. The development of an efficient and automatic RoI selection method has, therefore, been investigated in this thesis to attain two major requirements: (*i*) faster and accurate *RoI segmentation* and (*ii*) efficient *representation of the segmented RoI*. An Active Contour Model (ACM) based segmentation scheme is developed to effectively tackle intensity inhomogeneities and different shapes, sizes and locations of RoIs, and thereby, to automatically segment the RoIs with higher accuracy. Unlike the existing ACMs, two novel local images are constructed and fitted in the relative entropy based energy functional for better curve evolution and increasing robustness to noise and initialization. The energy equation is also scaled by local dispersion based edge mapped image for accuracy in boundary detection and smoothness. For the efficient representation of the segmented RoIs, the segmented region is defined by its original shape with reduced information by an effective polygonal decimation process. The overall performance of the proposed automatic RoI selection method is verified with the effectiveness and efficiency of the newly developed RoI segmentation and representation schemes for multi-modality MIs. Particularly, compared to the prominent and recent ACMs, the proposed segmentation scheme offers a faster curve evolution and more robustness to noisy, low-contrast, and intensity inhomogeneous MIs. The effective representation scheme is also compared with the 5 times and 10 times reduced vertices and respective bit requirements. The utilization of the proposed RoI selection method would be promising for the region-based MI processing and its security protection applications.

LIST OF TABLES

LIST OF FIGURES

LIST OF ABBREVIATIONS

ACM	Active Contour Model
ACWE	Active Contour without Edges
CT	Computed Tomography
DSA	Digital Subtraction Angiography
DSC	Dice Similarity Co-efficient
ESF	Edge Stopping Function
GAC	Geodesic Active Contour
HD	Hausdorff distance
JI	Jaccard Index
JND	Just Noticeable Distortion
JSC	Jaccard Similarity Co-efficient
LFI	Local Fitted Image
LHIF	Local Hybrid Image Fitting
LPF	Local Pre-Fitting
MG	Mammography
MHD	Modified Hausdorff Distance
MI	Medical Image
MR	Magnetic Resonance
PC	Piecewise Constant
RF	Radio Fluoroscopy
RoI	Region of Interest
RoNI	Region of non-interest
RSF	Region Scalable Fitting
SFI	Square Fitted Image
SPF	Signed Pressure Force
US	Ultrasound
WREP	Weighted Relative Entropy Pre-fitting

LIST OF SYMBOLS

I	An input image
Ω	The domain of input image, I
$\mathbb{R}^2$	Two dimensional set of real numbers, where Ω is a subset
E_{CV}	Energy with Chan-Vese model
λ_1, λ_2	Weight of energy equation
C_1, C_2	Global intensity averages in Chan-Vese model
H^ε	Approximated Heaviside function
μ	Weight of level set penalizing term
ν	Weight of Length regularizing term
C	Closed curve corresponds to zero Level set
ϕ	Level set function
ε	Smoothness controlling parameter of Heaviside function
σ	Standard deviation of Gaussian distribution
K_σ	A Gaussian kernel of standard deviation σ
W_K	Gaussian window of size K with local hybrid image fitting
f_1, f_2	Intensity averages inside a Gaussian window
E^{RSF}	Energy with region scalable fitting
δ_ε	Regularized Dirac function
m_1, m_2	Local intensity averages in local hybrid image fitting
I_{LFI}	Local fitted image
I_{SFI}	Square fitted image
E^{LHIF}	Energy with local hybrid image fitting
E^{LPF}	Energy with local pre-fitting
$\Omega_x, \Omega_s, \Omega_l$	Neighborhood around center pixel x in local pre-fitting model
f_m, f_s, f_l	Intensity pre-fitting functions with local pre-fitting
E^{WREP}	Energy with weighted relative entropy pre-fitting
S_r	Local intensity dispersion
Π_x	Local kernel to calculate intensity dispersion
I_{LPFI}	Local pre-fitted image
I_{SPFI}	Square pre-fitted image
$H(P)$	Entropy of the distribution P
$H(P,Q)$	Cross-entropy of two distributions, P and Q

CHAPTER 1

INTRODUCTION

1.1 Introduction

Medical Image (MI) is a specialized form of clinical and biological data and a vital part of modern heath-care services and clinical practice and research. The MIs generally contains two regions: region of interest (RoI) and region of non-interest (RoNI). The RoI has importance for medical procedures and practices, and the RoNI is the complementary part of RoI that does not have any clinical importance. Many MI applications, including digital watermarking required to preserve the RoIs to provide continuous security protection to the MIs. For example, content-authentication, copyright protection, integrity establishment, and annotation are a few that attracted much attention recently [1–13]. Those applications have additional requirements for the MI due to the inevitable distortion in the image introduced by the underlying processing techniques. These requirements are: (*i*) to ensure an acceptable level of embedding distortion in the image, and (*ii*) to provide continuous protection of the image [12, 14].

The first requirement ensures a confined distortion in the processed images. Failing to achieve this requirement may raise legal and ethical concerns of the medical professionals to use the processed images for any medical or clinical purpose [15]. To address this, many reversible (or loss-less) processing techniques have been developed that can restore the processed image to the original [12, 13, 16–18]. The later requirement, on the other hand, means that the security key or message has to always remain embedded to provide continuous protection of the image [19]. These two requirements, however, conflict with each other: if the processed image is restored to the original version, its security protection discontinues; if not, legal and ethical concerns arise. Region-based

processing has shown the potential to resolve this conflict [1–3, 5, 7, 10]. Before discussing the state of this research problem in light of the literature, the regions in MIs, their segmentation and representation are briefly discussed below.

1.1.1 Medical image (MI) regions

An MI can be differentiated with RoI and RoNI. The RoI in MI is the region that is important from the diagnosis point of view and should be preserved from any distortion caused by the security protection applications. Usually, RoI in MI is selected by medical practitioners, and thus, it may vary in MIs according to the requirement set by the physicians. Region-based processing requires to segment the image in RoI and RoNI first and then locate the RoI, representing it, and keeping the location information as a side information. An effective selection of RoI in region-based processing thus requires (*i*) its unsupervised and accurate segmentation and (*ii*) its representation with an RoI mask having location information.

1.1.2 Segmentation and representation of RoIs

The RoI segmentation is an ever-challenging task that separates clinically important regions from the unimportant regions in MIs. This is because, MIs can be of different modalities such as CT—Computed Tomography, MR—Magnetic Resonance, X-ray, DSA—Digital Subtraction Angiography, RF–Radio Fluoroscopy, US—Ultrasound, MG—Mammography, to name a few. Different modality MIs have different perceptual contents and random locations, shapes and intensity profile. Therefore, finding a suitable RoI segmentation scheme, in general, has remained an open challenge for all modality MIs. Despite this challenge, for region-based processing, an accurate segmentation is a prime requirement to avoid the risk of diagnosis and to minimize the legal and ethical concerns of the medical professionals.

An effective representation of RoIs is another important process to preserve

the RoI from any distortion. This representation scheme creates an RoI mask that captures the RoI and can locate it easily with a minimum side information. Generally, MIs have RoIs with different shapes, size, and locations. So, representing the RoI and locating it in the image with a general mask is not an effective solution for multi-modality MIs. Therefore, for the region-based processing and applications, an effective representation scheme requires to generate the mask according to the segmented RoI of different modality MIs.

1.2 Literature Review

The state-of-the-art schemes of RoI segmentation and representation and their potentials and limitations are reviewed in this section. In light of the limitations of the promising schemes, the research gap is identified and the objectives of this work are set thereby. The summary of the review is now presented below in two major sections: *(i)* RoI segmentation schemes, and *(ii)* RoI representation schemes.

1.2.1 RoI segmentation schemes

A number of segmentation schemes have been developed with different underlying principles. Popular segmentation schemes can be classified as follows: *edge-based* [20–22]; *thresholding-based* [23], *clustering-based* [24]; *region growing-based* [25]; and *active contour-based* [26–29]. Edge-based segmentation mainly employs different edge detection operators, for example, Roberts, Sobel, Laplacian, Prewitt, and Canny. These operators have different features and limitations [30]. For example, classical operators like Prewitt and Robert operators are simple and can detect edges and their orientation. However, these schemes are sensitive to noise. Zero crossing operators like Laplacian can detect edges and their orientation with some fixed directional characteristics, but remain sensitive to noises. Gaussian-based operators like Canny has separate considerations of error rate, edge localization, and response

with better signal to noise ratio. These schemes are usually complex and may have false zero crossings.

Thresholding-based schemes determine a threshold and separate pixels in two classes. In clustering schemes, the number of cluster centers is determined heuristically or randomly, and pixels are accommodated in clusters according to their intensity variations. Histogram-based schemes determine clusters in the image by peaks and valleys in the histogram. Region growing schemes determine clusters in an image by comparing neighboring pixels with a similarity criterion. If it is satisfied, then a particular pixel is inserted into a cluster of pixels. Region growing schemes can be broadly divided as seeded and un-seeded and are normally affected by noise.

In contrast to the above types of segmentation schemes, Active Contour Models (ACMs) [27–29, 31] have shown considerable efficiency in segmentation using different image features. Active contours are image feature guiding curves that evolve and deform its initial shape taking image information into consideration. These contours are also called Snakes because evolving contour actually slithers inside the image before surrounding the image object. Initial development of ACM-based models started with the parametric representation of the evolving contour. But, due to the problem of re-parameterization, self-intersection, failing to support internal boundaries, being trapped in the local minima, and sensitivity to location and shape of the initialized contours, ACM was improved by introducing inflating balloon force [32, 33] and level set representation of evolving contour [34, 35] with a geometric partial differential equation. Later, Caselles *et al*. [28] established the relation of energy minimization approach of classical Snakes with curve evolution approach of geometric active contours in Geodesic Active Contour (GAC) model. This approach is called GAC, because the underlying energy can be interpreted as the length of a contour in Riemannian space with a metric induced by the image intensity. These models used gradient-based edge defining and stopping functions to stop the curve propagation and remained prone to

the weak edge and local minima due to noise.

To address the limitations of the above ACMs, Chan and Vese proposed their pioneering Active Contour without Edges (ACWE) or CV model [29] with the variational level set formulation and Mumford-Shah functional. That model utilized two global intensity means as the region descriptors in the energy functional to properly segment the standard images. Since the model cannot detect intensity inhomogeneity and the other local variations and noise, subsequent developments of ACM studied the local region descriptors like the Region Scalable Fitting (RSF) [31] and Local Image Fitting (LIF) [36]. The RSF model used two local intensity fitting functions to define a Gaussian weighted energy functional, and the LIF model used image difference based energy functional to tackle the inhomogeneity. Those models had estimable capability of detecting inhomogeneity but remained affected by the noise and initialization.

Recently, the combined regional features with the edge descriptor have created a new paradigm of ACM for better initialization robustness and effective contour evolution. The Local Hybrid Image Fitting (LHIF) model [37] employed relative entropy (also called the Kullback-Leibler divergence) of two locally fitted images from the RSF and LIF models to define its energy functional. Despite improved accuracy, speed, and initialization robustness, that model remained sensitive to noise. The Local Pre-fitting (LPF) [38] model then introduced local approximations of intensity fitting terms to minimize the computational complexity of Gaussian convolution and to improve initialization, noise tolerance and contour-evolution speed. But, the LPF model was flawed with the additional contours generated at a higher iteration. The Entropy Weighted Fitting (EWF) [39] model has latterly used an entropy weighted energy functional to better tackle the inhomogeneity and enhance the object boundary.

An ACM-based scheme offers relatively higher accuracy in segmentation. It also provides the opportunity to include different image statistical features in the segmentation process to identify and isolate the desired RoI from the image. Although the above

ACMs have the potential for MIs, there is further room for improvement in terms of curve evolution speed and robustness to initialization, noise, low-contrast, and intensity inhomogeneity using a more efficient local feature estimation for the MIs.

1.2.2 RoI representation schemes

For region-based applications including *Digital Watermarking*, different approaches have been used to define the RoI masks to represent the RoIs. A few of them considered an automatic or semi-automatic segmentation of RoIs / RoNIs. For example, Coatrieux *et al*. [2] used morphological operation and threshold-based RoNI segmentation of MR images. Fotopoulos *et al*. [5] used a simple scanning and threshold-based scheme to automatically find the smallest possible rectangle capturing the whole head shape of a brain-MRI. Zhang *et al*. [9] proposed a block-energy-based scheme to determine the RoI of the original MIs. Fylakis *et al*. [40] used an RoI pixels' non-consecutive selection criteria based on the JND (Just Noticeable Distortion) for MRI and X-ray images. Al-Dmour and Al-Ani [8] utilized Otsu's threshold for partitioning the MR image into RoI and RoNI. Biswas *et al*. [41] employed fuzzy C-means, Sobel edge and Harris corner detection for RoI and RoNI segmentation for US and MR images. The above schemes are mainly used to segment RoIs for watermarking applications, but most of the literature disregard the efficiency in segmenting the RoI, which is an important requirement, as mentioned in Sec. 1.1.2.

Different shapes of RoI / RoNI have also been used to create the RoI masks. Mainly five types of general RoI shapes have been studied; namely, rectangle [1, 5, 40, 42, 43], polygon [7, 11], ellipse [44], circle [41] or combination of them [45]. Additionally, RoIs have also been defined using their segmented region, for example, using morphological processing [2], Otsu's threshold [8] and adaptive thresholding [9]. Many of the schemes used manual drawing by a radiologist to get RoI, making it a slow and inefficient process for large scale processing. Evidently many schemes are proposed

to select or represent RoIs in MIs, but selecting it efficiently with its actual shape preserved is not yet addressed.

1.3 Research Motivation

Recent developments in the area of MI processing and applications, as discussed in the previous section, suggest that the region-based processing can be an effective solution to minimizing the ethical concern raised for MI processing and security protection application, including digital watermarking. This solution, however, requires an accurate and automatic (or unsupervised) segmentation and representation of RoIs.

However, despite being an important pre-processing step, the segmentation and representation of RoIs for multi-modality MIs are not yet investigated with due importance. It is because, no single segmentation scheme is generally suitable for all modalities of MIs. RoIs are normally decided by the medical professionals and largely vary with the clinical and diagnosis requirement. Besides, RoIs in MIs normally vary a lot in shape, size, location, and intensity profile, and image segmentation schemes usually do not consider all those features available to detect a given RoI. Although the manual selection of RoIs by a radiologist is suggested by many researchers, it is inefficient and time-consuming, particularly when dealing with a large number of images. The success of these procedures entirely depends on humans, and sometimes wrongly perceived RoIs can lead to an incorrect diagnosis of a disease. The RoI segmentation and selection in MIs thus demand an automatic and efficient framework for their MI processing and applications.

The literature suggested different segmentation and selection schemes for different modalities of MIs and RoIs. This means that a segmentation scheme generally effective to the common modalities of MIs is unknown. Moreover, different types of shapes were used to represent RoIs, but an efficient RoI representation scheme is yet to be

developed that can capture RoI accurately with minimum possible side information.

In this research work, due importance is therefore given on developing a segmentation scheme that can work equally better than the existing schemes to segment RoIs in MIs with varying intensity profiles, complicated and noisy background and, multiple numbers of RoIs. Recall from the literature review section that an ACM-based segmentation can have the potential to attain the maximum requirements of segmenting MIs with the RoIs having varied intensity profile, shape, size, location, and quantity. So, the development of an RoI selection framework for region-based processing with a new ACM-based segmentation and dynamic RoI selection process is envisaged in this work.

1.4 Research Objectives

In light of the identified requirements of an efficient RoI selection method for multi-modality MIs, the specific objectives of this work are outlined as follows.

a) To investigate the state of RoI segmentation in MI watermarking to determine requirements for locating and representing RoI/RoNI during watermark embedding and extraction.

b) To select an existing segmentation scheme that can accurately locate RoI with minimum computational overheads.

c) To develop an efficient process to represent the segmented RoI using a set of minimum information.

d) To develop a method of RoI/RoNI selection combining the above segmentation and representation schemes (stated in b and c).

e) To carry out necessary implementations of the developed method for its performance evaluation and validation for multi-modality MIs.

The expected outcome of the proposed research is a new automatic RoI selection method that could accurately and effectively locate RoI before and after any region-based processing, including watermark embedding.

1.5 Organization of the Thesis

The remainder of this thesis is organized as follows.

Chapter 2 captures the background of the proposed research in two parts. In the first part existing and prominent ACM based segmentation schemes are discussed with their summarized technical details. These discussions also include possibilities for improvement in those schemes, creating further opportunities to develop an improved segmentation scheme. In the second part, different RoI representation schemes are discussed with the focus on their limitations and advantages towards developing an efficient RoI representation scheme.

Chapter 3 presents the gradual development of the proposed segmentation scheme highlighting its technical details and algorithmic development. It also includes the proposal of an efficient RoI representation for region-based MI processing and watermark embedding scenario.

Chapter 4 presents the performance of the proposed RoI selection method with the newly developed segmentation and selection schemes' performance compared to the related and recently developed segmentation schemes. The efficiency of the proposed RoI selection scheme in terms of side information required is also presented in this chapter.

Chapter 5 presents the conclusion of the thesis with a summary of the original contributions, significance, and future work.

CHAPTER 2

RELATED WORKS

2.1 Introduction

This section introduces the related works on which the research contribution presented in this thesis has been made. In Sec. 1.1.2 prominent segmentation schemes have been discussed with their important technical details, advantages, and limitations. Segmentation schemes used in popular region-based watermarking schemes and their comparison with ACM-based schemes are also briefly discussed at the end of that section. Besides, the RoI representation schemes for the region-based processing are briefly studied with their limitations and scope of further improvement in Sec. 2.3 . Subsequently, the identified limitations of both the segmentation and representation schemes are summarized with the option of possible developments (see Sec. 2.4)

Recall from Chapter 1 that the region-based processing has the potential to address ethical concern with the distortion in MIs and to ensure continuous protection of the MI-data. In region-based processing, the RoIs of MIs are segmented and preserved with the minimum information to represent and locate them accurately. Out of many prominent segmentation schemes, none of them has been tested for all the common modalities of MIs. It is because segmentation schemes usually work better for particular modalities of MIs. Unlike the counterpart, the ACM-based schemes can associate different image features, and thus have the potential to segment RoIs in multi-modality MIs as discussed in Chapter. 3. So, this chapter captures the framework of the promising ACM-based segmentation schemes.

Besides, the conventional schemes of RoI representation are analyzed. The conventional use of manual, automatic, and semi-automatic construction of RoI masks

with different shapes for RoI representation are not efficient enough for not using the actual shape of RoI. It is because, the representation and location of a complex RoI generates a mask undesirably including the RoNI in it, and increases the size of side information. Therefore, the scope of improving the RoI representation has also been investigated in this chapter in light of the conventional schemes.

2.2 Related RoI Segmentation Schemes

The RoI segmentation is an important step of a region-based MI processing and applications. The RoI should be segmented with higher accuracy to ensure that it does not include any part of the RoNI. Therefore, a segmentation scheme can generally be suitable for all the common modalities of MIs, if it is dynamic enough to accommodate maximum image features. Additionally, the scheme is to be robust against noise, intensity variation, weak edge problem in the low contrast and complex background images, and also can distinguish the multiple objects with similar intensity patterns. Recall from the previous chapter that the RoI varies with MI modalities and the images capturing different biological organs or parts. However, no such considerations can be tracked in the literature for the effective segmentation of RoIs.

Conventionally, manual drawing or selection by radiologist has been adopted in different MI applications [1,7,11,44]. These schemes are usually time-consuming and less efficient. For example, in Fig. 2.1, X-ray image of knee is shown to be represented by rectangular, elliptical, circular, combination of rectangles, and polygonal RoI using a manual drawing tool. It shows the complexity and inadequacy of representing RoIs by basic shapes. Besides, the thresholding-based scheme is also considered to differentiate RoI and RoNI, for example, using the Otsu's threshold in [8] and the heuristically selected thresholds by comparing background and foreground in [40,46]. For more effective segmentation, clustering-based scheme like Fuzzy C-means clus-

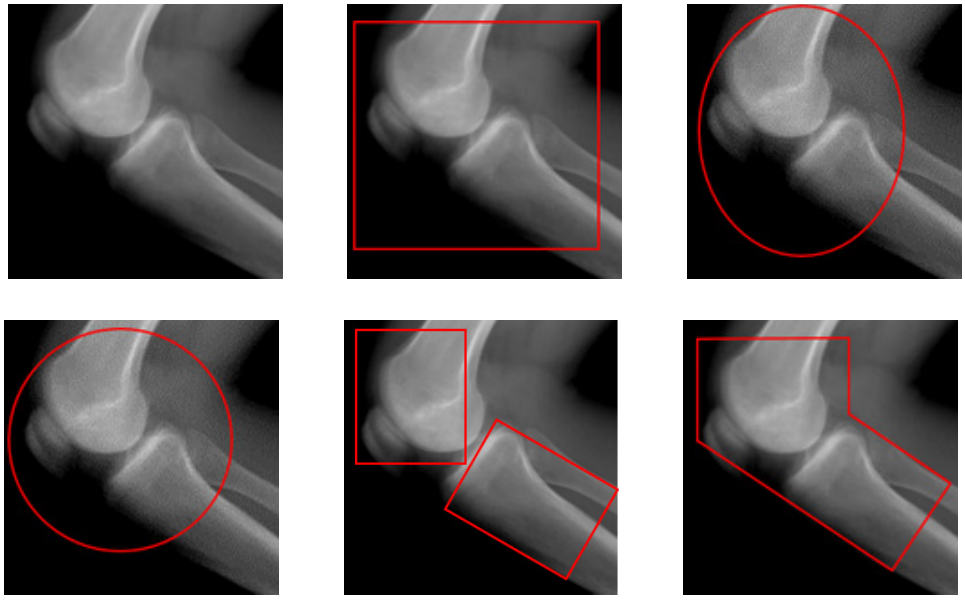

Figure 2.1: Manual selection of X-ray image of Knee

tering in [41] and the edge-based scheme like Canny edge in [47] have later been used. The above application-specific schemes demonstrated good results for the certain MI-modality, but they cannot be equally effective to a multi-modality MI application scenario. As discussed in Sec.1.2.1, an active contour based segmentation scheme can be more promising due to its dynamic consideration of image statistics. A few prominent and recent ACM-based segmentation schemes are now described below with their important technical details and scopes of improvement. These schemes are Chan & Vese (CV) model [29], Region Scalable Fitting (RSF) model [31], Local Hybrid Image Fitting (LHIF) model [37], and Local Pre-Fitting (LPF) model [38].

2.2.1 The Chen & Vese (CV) model

The Chan-Vese (CV) [29] is a region-based piecewise-constant active contour model. It aims at minimizing Mumford-Shah functional for segmentation and level sets assuming that the intensity in regions is constant or it exhibits homogeneity in regions. This model can achieve object boundaries even if the gradient is not prominent. It can stop evolving a curve without requiring edge-stopping functions based on the gradient

of the image. This model thus can effectively detect very smooth and discontinuous object boundaries. Generally, for an input image I, $I : \Omega \to \mathbb{R}^2$ and a level set, $\phi : \Omega \to \mathbb{R}^2$, this model minimizes the following energy functional in Eq.(2.1). A closed curve that corresponds to the zero level set is $C = \{x \in \Omega | \phi(x) = 0\}$. The fixed parameters, $\mu \geq 0, \nu \geq 0$, λ_1, $\lambda_2 > 0$ control the image feature driving force inside and outside of evolving contour. For images with smooth intensity λ_1 and λ_2 are usually equal.

$$\begin{aligned} E_{cv} = \lambda_1 \int_\Omega |I(x) - c_1|^2 H^\varepsilon(\phi)\, dx + \lambda_2 \int_\Omega |I(x) - c_2|^2 (1 - H^\varepsilon(\phi))\, dx \\ + \mu \int_\Omega |\nabla(H^\varepsilon(\phi))|^2 dx + \nu \int_\Omega H^\varepsilon(\phi) dx \end{aligned} \tag{2.1}$$

Additionally, the value of the level set is defined with the conditions in Eq. (2.2). A smooth and approximated version of the Heaviside function, $H^\varepsilon(\phi)$ is represented in Eq. (2.3) with a controlling parameter, ε. Ideally, $H^\varepsilon(\phi)$ is the unit step for $\varepsilon \to 0$. The parameter, μ controls the smoothness of zero level set and the constants, c_1 and c_2 approximate intensity of image inside and outside of the contour. For energy minimization with a fixed value of ϕ, c_1 and c_2 are calculated with Eq. (2.4a) and Eq. (2.4b).

$$C = \begin{cases} inside(C) = \{x \in \Omega \mid \phi(x) > 0\} \\ outside(C) = \{x \in \Omega \mid \phi(x) < 0\} \\ on(C) = 0 \qquad\qquad \text{otherwise} \end{cases} \tag{2.2}$$

$$H^\varepsilon(\phi) = \frac{1}{2} + \frac{1}{\pi} arctan(\frac{\phi}{\varepsilon}) \tag{2.3}$$

$$c_1(\phi) = \frac{\int_\Omega I(x) \cdot (H^\varepsilon(\phi)) dx}{\int_\Omega H^\varepsilon(\phi)\, dx} \tag{2.4a}$$

$$c_2(\phi) = \frac{\int_\Omega I(x) \cdot (1 - H^\varepsilon(\phi)) dx}{\int_\Omega (1 - H^\varepsilon(\phi)) dx} \tag{2.4b}$$

Re-initialization of ϕ is required in conventional level-set methods to keep it close to a signed distance function. CV model attained the re-initialization requirement with a regularizing term to keep the zero level set close to a signed function. This term penalizes the dislocation of level set function from signed function and regularizes it to obtain the desired contour eventually. Keeping c_1 and c_2 fixed, the energy functional is minimized with respect to ϕ by solving the gradient flow equation as in Eq. (2.5)

$$\frac{\partial \phi}{\partial t} = \delta_\varepsilon(\phi)\left[-\lambda_1\left(I(x)-c_1\right)^2 + \lambda_2(I(x)-c_2)^2 + \mu\ \mathrm{div}\left(\frac{\nabla\phi}{|\nabla\phi|}\right) - \nu\right] \tag{2.5}$$

The CV model works fine for images with no local intensity variations. As intensity inhomogeneity is a local phenomenon, CV model fails to segment objects that can not be represented by global intensity descriptors. In the case of multi-modality MIs, CV model fails to provide local segmentation and can not identify important image objects with a large difference from the global intensity means.

2.2.2 The region scalable fitting (RSF) model

The Region Scalable Fitting (RSF) [31] model was proposed to identify local variations in images. Unlike CV model, it considered local intensity averages in a Gaussian kernel inside and outside of the evolving contour. The RSF model defined an energy functional with two local intensity fitting functions. Thus, the RSF energy functional given in (2.6a) infuses the weighted local features of the neighboring pixels of a kernel's center, which enables the model to segment images with local intensity variation. Here, the energy terms are confined by the zero level set, ϕ, which is negative-, positive- and zero-valued function inside, outside, and on the contour C, respectively.

A smooth approximation of Heaviside function $H^\varepsilon(\phi) = \frac{1}{2} + \frac{1}{\pi} arctan(\frac{\phi}{\varepsilon})$ is used to define two sides of the contour denoted by $M_1^\varepsilon(\phi(y)) = H^\varepsilon(\phi)$ and $M_2^\varepsilon(\phi(y)) = 1 - H^\varepsilon(\phi)$. The weights of energy functional outside and inside the initial

contour are λ_1 and λ_2; the optimally approximated intensity values outside and inside the contour are $f_1(x)$ and $f_2(x)$ defined in (2.6b) and (2.6c); and K_σ is the Gaussian kernel with the location of its center pixel, x. The scale parameter to the region of influence of the Gaussian kernel or its standard deviation is σ. Additionally, that energy functional incorporates popularly used length regularizing term and level set penalizing term with the weights, ν and μ, respectively.

$$E^{RSF} = \sum_{i=1}^{2} \int \lambda_i \left(\int_\Omega K_\sigma(x-y) \left| I(y) - f_i(x) \right|^2 M_i^\varepsilon(\phi(y)) dy \right) dx + \nu \int |\nabla H(\phi(x))| \, dx + \mu \int \frac{1}{2} (\nabla \phi(x) - 1)^2 dx \tag{2.6a}$$

$$\text{where, } f_1(x) = \frac{\int_\Omega K_\sigma(x-y) \left[I(y) \cdot H^\varepsilon(\phi(y)) \right] dy}{\int_\Omega H^\varepsilon(\phi(y)) \, dy} \tag{2.6b}$$

$$f_2(x) = \frac{\int_\Omega K_\sigma(x-y) \left[I(y) \cdot (1 - H^\varepsilon(\phi(y))) \right] dy}{\int_\Omega (1 - H^\varepsilon(\phi(y))) dy} \tag{2.6c}$$

The initialized contour then evolves with the gradient flow in (2.7) obtained from the energy functional in (2.6a) using the standard gradient descent method with a set of fixed values of f_1 and f_2 for a given ϕ.

$$\frac{\partial \phi}{\partial t} = -\delta_\varepsilon(\phi)(\lambda_1 e_1 - \lambda_2 e_2) + \nu \delta_\varepsilon(\phi) \, \text{div}\left(\frac{\nabla \phi}{|\nabla \phi|} \right) + \mu \left(\nabla^2(\phi) - div\left(\frac{\nabla \phi}{|\nabla \phi|} \right) \right) \tag{2.7}$$

$$\text{where, } \delta_\varepsilon(x) = \frac{\partial H^\varepsilon(\phi)}{\partial t} = \frac{\varepsilon}{\pi(\varepsilon^2 + x^2)}$$

$$e_i = \int_\Omega K_\sigma(x-y) \left| I(x) - f_i(y) \right|^2 dy \quad \text{for all } i \in \{1,2\}$$

Therefore, the RSF model can segment the images accurately with local variations. However, the model can easily be flawed by the local minima, noise, and the contours initialized far away from the desired boundary. Initializing in strong inhomogeneity or noise affected region often leads to undesired contour evolution. However, The initialization robustness can be improved by increasing the scale parameter and Gaussian kernel size resulting in inaccurate segmentation and higher iteration time. In

other words, if the initial contour is not placed properly or far from the desired object boundary the model either becomes slow or it segments inaccurately.

2.2.3 The local hybrid image fitting (LHIF) model

The Local Hybrid Image Fitting (LHIF) model [37] is developed to combine the potentials of the two locally fitted images of RSF models. Close observation of RSF energy in (2.9a) reveals that, two locally fitted images can be constructed from the energy functional. The local fitted image (LFI), I_{LFI} in (2.8a) is constructed from the average intensities, m_1 and m_2 in (2.8c) and (2.8d) in the region defined by Gaussian window, W_k with the standard deviation of σ and the radius of k. Additionally, a square fitted image (SFI) is constructed in (2.8b) to reduce the effect of noise. Intensity averages in (2.8c) and (2.8d) are actually the same as used in RSF model in (2.6b) and (2.6c) in a Gaussian window. Those two local images, I_{LFI} and I_{SFI} are then introduced in the RSF energy using (2.9a) to define the LHIF energy in (2.9b) by employing relative entropy-based dissimilarity measurement in between the original image and its local approximations.

$$I_{LFI} = m_1 M_1^{\varepsilon}(\phi) + m_2 M_2^{\varepsilon}(\phi) \tag{2.8a}$$

$$I_{SFI} = \sum_{i=1}^{2} m_i^2 M_i^{\varepsilon}(\phi) \quad \text{for all } i \in \{1,2\} \tag{2.8b}$$

$$m_1 = mean\left(I \in (\{x \in \Omega | \phi(x) < 0\} \cap W_k(x))\right) \tag{2.8c}$$

$$m_2 = mean\left(I \in (\{x \in \Omega | \phi(x) > 0\} \cap W_k(x))\right) \tag{2.8d}$$

$$\begin{aligned} E^{RSF} &= \sum_{i=1}^{2} \lambda_i \iint K_\sigma(x-y)\left[I^2(y) - 2I(y)m_i + m_i^2\right] M_i^{\varepsilon}(\phi) dydx \\ &= \int\int K_\sigma(x-y)\left[I^2(y) - 2I(y)I_{LFI}(x) + m_1^2 M_1^{\varepsilon}(\phi) + m_2^2 M_2^{\varepsilon}(\phi)\right] dydx \end{aligned} \tag{2.9a}$$

$$E^{LHIF} = \lambda_1 \int \left[I(x) \log \left(\frac{I(x)}{I_{LFI}(x)} \right) + I_{LFI}(x) \log \left(\frac{I_{LFI}(x)}{I(x)} \right) \right] dx$$
$$+\lambda_2 \int \left[I^2(x) \log \left(\frac{I^2(x)}{I_{SFI}(x)} \right) + I_{SFI}(x) \log \left(\frac{I_{SFI}(x)}{I^2(x)} \right) \right] dx \quad (2.9b)$$

$$\frac{\partial \phi}{\partial t} = \delta_\varepsilon(\phi)(\lambda_1 e_1 + \lambda_2 e_2) + \nu \delta_\varepsilon(\phi) div \left(\frac{\nabla \phi}{|\nabla \phi|} \right) + \mu \left(\nabla^2(\phi) - div \left(\frac{\nabla \phi}{|\nabla \phi|} \right) \right) \quad (2.10a)$$

$$e_1 = (m_1(x) - m_2(x)) \left(\frac{I(x)}{I_{LFI}(x)} - 1 - \log \frac{I_{LFI}(x)}{I(x)} \right) \quad (2.10b)$$

$$e_2 = \left(m_1^2(x) - m_2^2(x) \right) \left(\frac{I^2(x)}{I_{SFI}(x)} - 1 - \log \frac{I_{SFI}(x)}{I^2(x)} \right) \quad (2.10c)$$

The LHIF model utilized two local fitted images and relative entropy in energy functional to suppress the complex image background and identify textural variations. The segmentation performance of the model in terms of initialization robustness, speed, and accuracy was significantly improved. Yet, the model is sensitive to noise that affects the residual error in local fitted images. It is difficult to set weighting parameters of intensity terms in (2.9b) derived from LFI and SFI of LHIF model. Sometimes the wrong selection of weight for the second term includes background information in segmentation result. So, the weight of the second term is more sensitive to the variation and should be chosen intelligently.

2.2.4 The local pre-fitting (LPF) model

The LPF model [38] proposed to expedite the curve evolution by approximating the intensity fitting terms locally prior to the curve evolution. Those terms were pre-fitted with the energy functional. In this sense, local pre-fitting functions do not have any relation with the level set formulations. They are calculated and added as a pre-processing stage. The local pre-fitting functions are defined in (2.11), where f_s and f_l are the local approximations of intensity averages given in (2.6b) and (2.6c), and Ω_x is a small

neighborhood of the center pixel's location, x. The local region, Ω_s defines the region of pixel values smaller than the mean value. Similarly, the local region, Ω_l defines the region of pixel values greater than the mean value. These two images are actually constructed from the main image, so they can be considered as the subset of the main image. Utilizing the locally calculated intensity average, the LPF energy functional was developed as in (2.12) and solved from the gradient flow equation in (2.13a).

$$f_m(x) = \text{mean}\left(I(y)|y \in \Omega_x\right) \tag{2.11a}$$

$$f_s(x) = \text{mean}\left(I(y)|y \in \Omega_s\right) \tag{2.11b}$$

$$f_l(x) = \text{mean}\left(I(y)|y \in \Omega_l\right) \tag{2.11c}$$

$$\begin{aligned} E^{LPF} = &\int_\Omega \left(\int_\Omega K_\sigma(x-y) \left|I(y) - f_s(x)\right|^2 H^\varepsilon(\phi) dy \right) dx \\ &+ \int_\Omega \left(\int_\Omega K_\sigma(x-y) \left|I(y) - f_l(x)\right|^2 \left(1 - H^\varepsilon(\phi)\right) dy \right) dx \end{aligned} \tag{2.12}$$

$$\frac{\partial \phi}{\partial t} = -\delta_\varepsilon(\phi)(e_s(x) - e_l(x)) + \nu \delta_\varepsilon(\phi) div\left(\frac{\nabla \phi}{|\nabla \phi|}\right) + \mu\left(\nabla^2(\phi) - div\left(\frac{\nabla \phi}{|\nabla \phi|}\right)\right) \tag{2.13a}$$

$$e_s = \int_\Omega K_\sigma(x-y) \left|I(y) - f_s(x)\right|^2 dx \tag{2.13b}$$

$$e_l = \int_\Omega K_\sigma(x-y) \left|I(y) - f_l(x)\right|^2 dx \tag{2.13c}$$

The LPF model minimizes the iteration time by reducing the use of Gaussian kernel convolution in calculating intensity fitting functions. The initialization robustness was also improved. It also reduces noise and enhances image contrast. Computational complexity is also less than original RSF model. But, the segmentation accuracy of the model is not impressive for the images with complex background.

2.3 Related RoI Representation Schemes

The RoI representation schemes adopted in prominent region-based data hiding applications are now reviewed. A crucial part of efficient RoI selection is RoI representation. Once the desired RoI is segmented from the MI, the subsequent challenge is to represent it. As the main focus of this research is to develop an efficient RoI selection method for the region-based MI processing and applications, we restrict our discussion to the RoI representation schemes used in the major region-based applications like digital watermarking. The limitations and scopes of possible developments of those schemes are also investigated.

An RoI representation scheme requires the boundary information to accurately locate it in a given MI. In other words, the accuracy of representation also depends on the accuracy of the segmented RoI. Thus, both the shape and location related information are required for this purpose. A minimum set of information is often required in MI applications that embed this information along with the other metadata. Thus, to preserve more room for the metadata, the representation information is desirably to be minimum. Additionally, minimizing this set of information without deteriorating the RoI shape is another challenge.

In most of the cases, region-based processing and applications utilized very basic shape representation of RoI to make it very simple. Despite being simple enough, those shapes are yet to be effective for the complicated and multiple RoIs in a single MI. For example, the rectangular, elliptical, polygonal and circular shapes have been used to represent RoI. In [45], elliptical, and rectangular shapes have been utilized, and in [47] and [48], examples of using irregular shape of RoI can be tracked. Additionally, RoIs have also been defined using their segmented region, for example, using morphological processing [2], Otsu's threshold [8] and adaptive thresholding [9]. Some schemes simply relied on manual selection of RoI / RoNI by the radiologist or a computer-aided

Table 2.1: Summary of RoI / RoNI Considerations in Region-based MI Processing

RoNI shape	Work	MI Modality	MI Segmentation				Remarks
			Input	Output	Setting	Principle	
Rectangular	Fotopoulos *et al.* [5]	MR (brain)	Image and manual threshold	Location map of RoI / RoNI	Semi-automatic	Thresholding with horizontal and vertical pixels' groups specifies an RoI	• RoI is embedded in RoNI • Location map is required • Threshold is manually selected
	Fylakis *et al.* [40]	MR and X-Ray	Image and length payload	RoI as a rectangle containing the imaged tissue	Manual	RoI is heuristically separated from the background	• Both RoI and RoNI is used for embedding • LSBs of RoI is used for data embedding • Original LSBs of RoI is embedded in RoNI
	Navas *et al.* [42]	X-Ray, MR and CT	Image	Diagonal vertices of RoI rectangle	Manual	Background is considered as RoNI	RoNI is used for embedding
	Rahimi *et al.* [43]	CT and MR	Image	Coordinates of rectangle of RoI	Automatic	Image background is considered RoNI and excluded in the RoI rectangle	• Both RoI and RoNI is used for embedding
	Pandey *et al.* [1]	Eye image	Image	Segmented RoI	Manual	RoI is defined with rectangular shapes	• RoNI is used for embedding
Elliptical	Menom *et al.* [44]	CT, US, MR and X-Ray	Image	Isolated RoI and scrambled RoNI	Manual	Logical ellipse based RoI representation	• Only RoNI is used for embedding
Elliptical / Rectangular	Al-Dmour and Al-Ani [45]	MRI	Image	Initial coordinates and size of RoI	Manual	Four element vector method specifies RoI with its initial coordinates and size	• Only RoNI is used for embedding
Circular	Biswas *et al.* [41]	MRI and IVUS	Binary image	Sample image with marked RoI and RoNI	Semi-automatic	Fuzzy C-means, Sobel edge, and Harris corner based scheme specifies a circular RoI	• Only selected RoNIs are used for embedding
Polygonal	Al-Haj and Amer [11]	MR, US and X-Ray (Grayscale MI)	Image	Partitioned image of non-overlapped blocks	Manual	Polygon-mask drawn by a radiologist defines RoI	• Both RoI and RoNI are used for embedding • RoI is used for reversible embedding
	Guo and Zhuang [7]	CT, MR and US	Image	Vertex information of selected polygonal RoI	Manual	Polygon-mask drawn by a radiologist defines RoI	• Outside of RoI is used for embedding
RoI Outline or Silhouette	Coatrieux *et al.* [2]	MR (head)	Averaged Image	RoNI location detected image	Automatic	Morphological operation with a threshold	• Both RoI and RoNI are used for embedding
	Zhang *et al.* [9]	Not specified	Image	RoI detected image	Automatic	Block energy-based scheme with an adaptive threshold T determines e RoI	• Only RoI is used for embedding
	Al-Dmour and Al-Ani [8]	MR	Image and Otsu's threshold	RoI selected image	Semi-automatic	Binarizing and segmenting the image with Otsu's threshold	• Only RoI is used for embedding • Rectangular RoI-mask is used

selection tool. Pandey *et al*. [1] employed a manual selection of RoI / RoNI of rectangle shape for digital eye image. Al-Haj and Amer [11] used a manual selection of RoI / RoNI of a polygon shape for MR, US, and X-Ray gray-scale images. Guo and Zhuang [7] employed similar manual selection of polygon-shaped RoI for CT, MR and US images. Memon *et al*. [44] also used manual segmentation of ellipse-shaped RoI for CT, US, X-Ray, and MR images. In [48] for ultrasound and MR images, manual selection of RoI was done. A summary of the RoI representation in existing MI processing literature is given in Table. 2.1.

The above conventionally used representation schemes of RoI usually missed a part of RoI leaving it in RoNI or they remained in-efficient to provide with a maximum possible RoNI as the room for the metadata embedding. Therefore, there is much room for the development of an efficient RoI representation scheme. Particularly, a decimation process has never been used and can be promising for this development, which will be presented in the following chapter.

2.4 Chapter Summary

This chapter captures the state-of-the-art schemes of both the segmentation and representation of RoIs. In some cases, basic segmentation schemes were used with limited performance in a specific MI modality application. Manual selection of RoIs with easily represented shapes and clustering-based schemes are also used. In summary, this chapter narrowed down the scope of developing a segmentation scheme with an ACM considering the MI-specific image features to capture the RoIs effectively. Additionally, the representation of the segmented RoIs can be more effective using a decimation process preserving its original shape and representing it with a minimum possible information, which are presented in the following chapter.

CHAPTER 3

PROPOSED ROI SELECTION METHOD

3.1 Introduction

An automatic and efficient RoI selection in MIs requires suitable segmentation and selection schemes for accurately segmenting the RoIs followed by their efficient representation. The segmentation scheme is to be equally effective for all modalities of MIs. But, with the random location, shape, size, and intensity and edge patterns, segmentation of RoIs from their background has remained as an open challenge. This means that the segmentation scheme should consider small intensity differences, weak or blurred edges of the RoI, and complex background of the image to be effective for different modality MIs. Recall from the previous chapter and Sec. 1.2 that the ACM-based segmentation can be promising for the MI image segmentation. Despite the significant segmentation accuracy, the performance of the recent ACMs, however, leaves much room for improvement in terms of the contour evolution speed and the robustness against the initialization, noise and intensity-inhomogeneity.

A new ACM is thus developed and presented in this chapter for the RoI segmentation. The pre-fitting functions of the LPF model are utilized to make the proposed model time-efficient and robust to noise, initialization. To expedite the curve evolution and to detect dissimilar regions accurately, the energy functional is defined using relative entropy estimations of the original image and two local fitted images calculated from pre-fitting functions. The energy functional is also weighted using a local dispersion based edge mapped scaling parameter to include local edge information in it. The gradient flow equation is calculated and iterated in variational calculus and Level set formulation for the expected boundary of RoI.

Additionally, for the efficient representation of the segmented RoI, a contour-point decimation approach has been utilized. Particularly, a basic distance offset error based decimation scheme is proposed, which discards a contour point for being smaller than a specified tolerance parameter. The segmented region thus can be represented by its original shape with less possible information to decrease the amount of pay-load required to relocate the RoI. The proposed method would thus provide with an RoI automatically segmented and represented, which can be used in different region-based imaging applications of MIs.

3.2 An Improved RoI Segmentation Scheme

A new ACM-based segmentation scheme is developed using a new Weighted Relative Entropy Pre-fitting model, which is called the WREP model in this thesis. As discussed in Sec. 2.2, the LHIF model can detect local variations using two locally fitted images and relative entropy measures. That model is noise sensitive as the noise increases residual errors in approximating locally fitted images. The LPF model, in contrast, improved the initialization robustness, speed of curve evolution, and noise withstanding capability, yet the problem of extra contour generation exists in that model. Moreover, only using intensity difference in contour evolution of that model leaves room for improvement with more effective use of local image features.

The proposed WREP model combines the potentials of the LHIF and LPF models by utilizing the relative entropy fitting energy. Moreover, to stop contour evolution on the object boundary, the energy functional is scaled with edge mapped image calculated from the estimated local dispersion. Local fitted images are used to detect local variations, but they are constructed using the intensity pre-fitting functions without Gaussian convolution for time efficiency, noise tolerance, and initialization robustness. The energy functional is defined in terms of relative entropy in between pre-fitted local

images and original image, allowing faster curve evolution in dissimilar regions. The intensity fitting functions of LPF found in (2.11) are actually local approximations of intensity averages in the LHIF model in (2.8d). So, the locally calculated pre-fitting functions in (2.11) are employed for better speed and noise tolerance. These processing steps and considerations are discussed below with more technical details and mathematical framework.

3.2.1 Two new local fitted images

A set of two new local fitted images are constructed and included in the proposed WREP model by using pre-fitting functions. These local images are called the local pre-fitted image (LPFI), I_{LPFI}, and the square pre-fitted image (SPFI), I_{SPFI} in our model, and given in (3.1a) and (3.1b). Unlike the local images, I_{LFI} and I_{SFI} defined in (2.8a) and (2.8b) in earlier schemes (see Sec. 2.2.3), the construction of I_{LPFI} and I_{SPFI} relies on pre-fitting functions for the local fitted images. These images are actually local approximations of the original image, and thus, they are less noisy, and their contrast is also enhanced. Besides, the intensity pre-fitting functions are calculated from the Gaussian average of the original image. So, re-constructed local images from intensity pre-fitting functions offer noise tolerance, contrast enhancement, and initialization robustness.

$$I_{LPFI} = f_s M_1^{\varepsilon}(\phi) + f_l M_2^{\varepsilon}(\phi) \tag{3.1a}$$

$$I_{SPFI} = f_s^2 M_1^{\varepsilon}(\phi) + f_l^2 M_2^{\varepsilon}(\phi) \tag{3.1b}$$

3.2.2 Redefined energy functional with relative entropy

The local energy functional of the proposed model is redefined with the relative entropy of two local fitted images with the original image to maximize the use of local intensity statistics. Relative entropy (also called Kullback-Leibler divergence) measures the difference of approximate probability distribution from a reference prob-

ability distribution. The value of relative entropy being zero indicates the distributions to be identical. If P and Q are two distributions, then the relative entropy or Kullback-Leibler (KL) divergence is defined as in Eq. 3.2a. Here, p and q are the probability densities of P and Q and x is a random variable. It is also the difference between entropy of a distribution P and its cross-entropy with another distribution Q as given in Eq. 3.2b. Here, $H(P,Q)$ is cross-entropy in between P and Q, while $H(P)$ is the entropy of P. It can be termed as expectation of log difference of probabilities in original distribution and approximate distribution. Some well-known properties of relative entropy are given below.

(*i*) The KL divergence or the relative entropy is always greater than zero.

(*ii*) It is additive for independent distribution.

(*iii*) Relative entropy measures is not symmetric. So, $D_{KL}(P \parallel Q) \neq D_{KL}(Q \parallel P)$.

(*iv*) To make it symmetric $D_{KL}(P \parallel Q)$ and $D_{KL}(Q \parallel P)$ can be added together. These are called mean seeking and mode seeking or forward and reverse Relative entropy respectively.

$$D_{KL}(P \parallel Q) = \int p(x)\log\left(\frac{p(x)}{q(x)}\right) dx \tag{3.2a}$$

$$\begin{aligned} D_{KL}(P \parallel Q) &= \int p(x)\log p(x)\, dx - \int p(x)\log q(x)\, dx \\ &= H(P,Q) - H(P) \end{aligned} \tag{3.2b}$$

$$\begin{aligned} E^{WREP} = \lambda_1 \int \left[I(x)\log\left(\frac{I(x)}{I_{LPFI}(x)}\right) + I_{LPFI}(x)\log\left(\frac{I_{LPFI}(x)}{I(x)}\right)\right] dx \\ + \lambda_2 \int \left[I^2(x)\log\left(\frac{I^2(x)}{I_{SPFI}(x)}\right) + I_{SPFI}(x)\log\left(\frac{I_{SPFI}(x)}{I^2(x)}\right)\right] dx \end{aligned} \tag{3.2c}$$

In the proposed WREP model, thus the dissimilarity among original image and I_{LPFI} and I_{SPFI} images are measured using Relative entropy. This estimation is the driving force of the proposed scheme and utilized to define the energy functional in

Eq. 3.2c. To make the energy symmetric, the forward and reverse both entropy are added. Also, using additive property, Relative entropy estimation of the original image with I_{LPFI} and I_{SPFI} both are added with two different weighting parameters.

3.2.3 A new edge scaling with local dispersion

The edge mapped image is newly included as an edge weighting parameter in the proposed energy functional using local dispersion estimation. The Dispersion of an intensity value from the mean intensity is called the standard deviation. The local standard deviation shows the dispersion of pixel intensities from the mean in a local region. So, the standard deviation, by definition, has higher intensity values at the edge showing higher dispersion from the local mean. This feature is used to extract edge information from the image and associated with the energy functional as a scaling factor. Moreover, local standard deviation reduces the effect of Gaussian noise and increases noise tolerance of the model. Therefore, a sliding window of size $r \times r$: $\Pi_x = \{y : |x-y| \leq r\}$ is defined to calculate local intensity dispersion, $S_r(x)$ for a kernel, Π_x having a center pixel location, x, and radius, r from the center in the neighborhood. Finally, an edge mapped image is obtained from the local dispersion of all the pixels with Bessel's correction in a neighborhood Π_x using (3.3). Here, $|\Pi_x|$ is the cardinality or number of the elements in the local window, and $\overline{\Pi_x}$ is the mean intensity of the window.

$$S_r(x) = \sqrt{\frac{\sum(y-\overline{\Pi_x})^2}{|\Pi_x|-1}} \tag{3.3}$$

$$\begin{aligned} E^{WREP} = \lambda_1 \int \left[I(x)\log(\frac{I(x)}{I_{LPFI}(x)}) + I_{LPFI}(x)\log(\frac{I_{LPFI}(x)}{I(x)}) \right] S_r(x)dx \\ +\lambda_2 \int \left[I^2(x)\log(\frac{I^2(x)}{I_{SPFI}(x)}) + I_{SPFI}(x)\log(\frac{I_{SPFI}(x)}{I^2(x)}) \right] S_r(x)dx \end{aligned} \tag{3.4}$$

Now, a local-dispersion scaled relative entropy-based energy functional is defined in (3.4) by two locally fitted images in (3.1a) and (3.1b) and the original image.

3.2.4 Contour evolution with the level-set

The contour evolves with the gradual change in the energy defined by the flow equation. For this, the energy functional is solved iteratively from the flow equation in (3.5a), where (3.5b) and (3.5c) shows the energy equations. A length regularizing term and level set regularizing term with weight ν and μ are also included in the energy-flow equation.

$$\frac{\partial \phi}{\partial t} = \delta_\varepsilon(\phi)(\lambda_1 e_1 + \lambda_2 e_2)\, S_r(x) + \nu \delta_\varepsilon(\phi) div\left(\frac{\nabla \phi}{|\nabla \phi|}\right) + \mu\left(\nabla^2(\phi) - div\left(\frac{\nabla \phi}{|\nabla \phi|}\right)\right) \quad (3.5a)$$

$$e_1 = (f_s(x) - f_l(x))\left(\frac{I(x)}{I_{LPFI}(x)} - 1 - \log\frac{I_{LPFI}(x)}{I(x)}\right) \quad (3.5b)$$

$$e_2 = \left(f_s^2(x) - f_l^2(x)\right)\left(\frac{I^2(x)}{I_{SPFI}(x)} - 1 - \log\frac{I_{SPFI}(x)}{I^2(x)}\right) \quad (3.5c)$$

In summary, with the new pre-fitted images and local-dispersion infused edge scaling in the WREP functional, the proposed ACM is expected to have faster curve evolution, robust initialization, efficient local variation detection, better noise tolerance, and excellent time efficiency.

3.3 A New RoI Representation Scheme

An efficient RoI representation is identified as the other requirement of the proposed RoI selection method. To represent the segmented region efficiently with its original shape, the contour points of the segmented RoI are calculated directly from the segmented region. The original contour points of RoI shape is also stored in order to locate it before and after MI processing successfully. This information is saved as a side information in the RoNI and reduces the storage space if it is large. So, in the proposed scheme, the number of vertices is dynamically reduced without compromising the original shape of the RoI.

A contour-point decimation is thus studied to effectively eliminate relatively less

significant vertex points in creating the RoI shape. It calculates the distance offset error of potential new edge points of the RoI shape. After that, the closest points of current vertices to the newly constructed edges are calculated. The distances of the initial contour points and the new contours points are now calculated. These distances are compared with the tolerance level set by the user, and the particular vertex point is discarded for being smaller than the tolerance. The tolerance level is set in a way so that, removing a particular vertex does not hamper the RoI so much to distort its original shape with precious clinical information. This process is continued until and unless the number of vertex does not come down to the desired lowest value without compromising the original shape of the RoI. The main procedure of the proposed contour point reduction is summarized below.

Step 1: For every vertex, the boundary offset errors are computed.

Step 2: All vertices are ordered in increasing order of error.

Step 3: The vertices with the lowest errors are removed.

Step 4: The errors between the two vertices adjacent to the deleted vertex are recomputed and accumulated.

Step 5: The *Step 2* to *Step 4* are repeated until no further vertices can be removed or the number of vertices has reached a user-defined value.

The output of the above steps is illustrated in Fig. 3.1. The original RoI requires 431 vertices in *top* row, which can be reduced to 86 after 5 times decimation in the *left* column of the *middle* row. With further decimation of 10 times, the number of vertices can be of only 43, as illustrated in the *right* column of the same row. The effect of reducing the vertices number for 15 times and 20 times are also shown in the *bottom* row, in the *left* and *right* columns. Detail results of this representation are given in

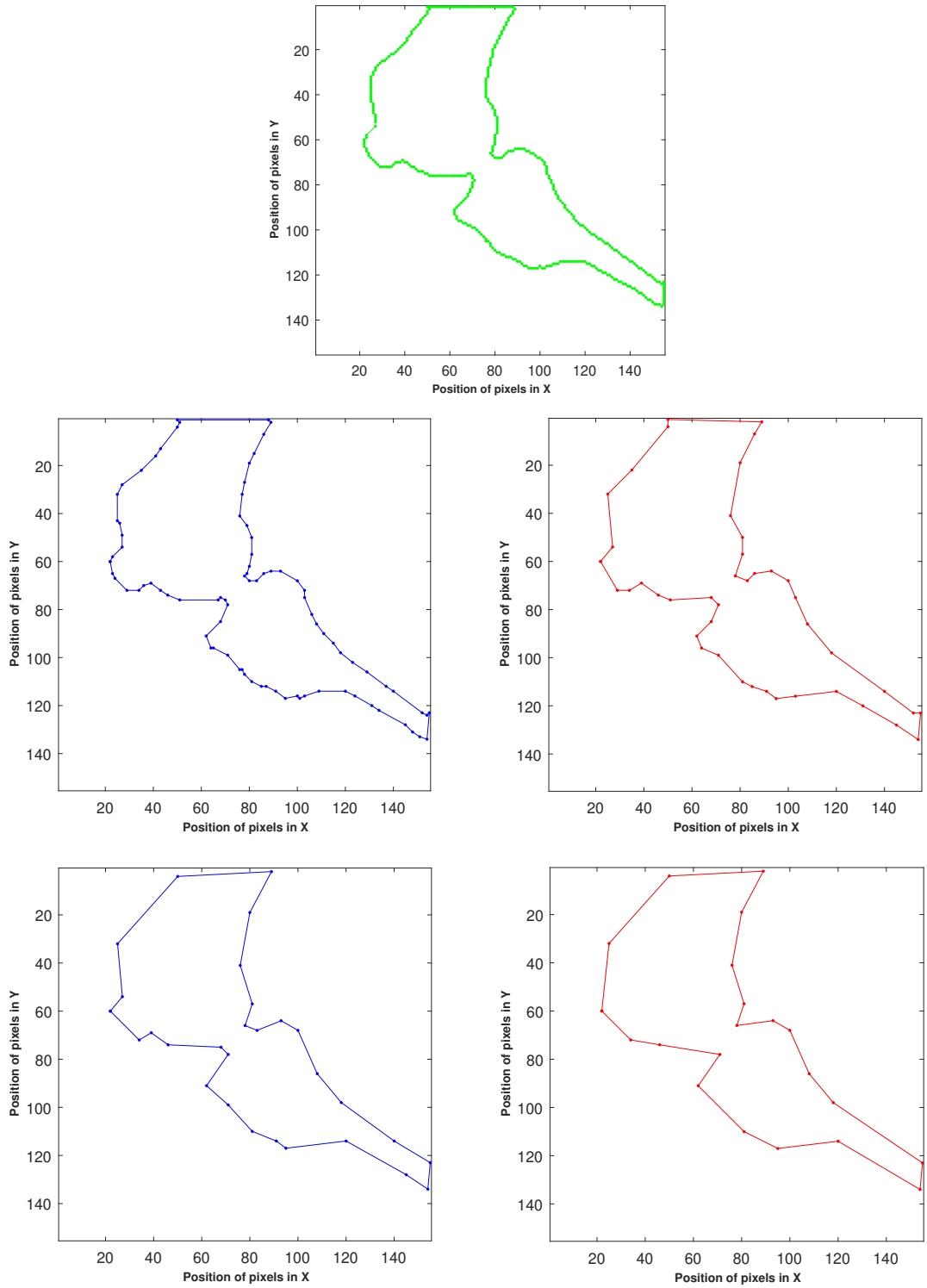

Figure 3.1: Example of outputs of the proposed RoI selection scheme for the segmented RoIs

Table 3.1: Reduction of bit requirement for RoI representation

Test Image	Original Vertices	Bit Required	Reduction	New Vertices	Bit Required
X-ray Knee (155 × 155)	431	6896	10 times	43	688
			15 times	29	464
			20 times	22	352

the following chapter. With the decreasing vertices number, the detailed shape of segmented RoI becomes an approximation of the original shape, which can be named as the basic shape of the original RoI. The bit requirements to represent the RoI with this decimation are shown in Table. 3.1.

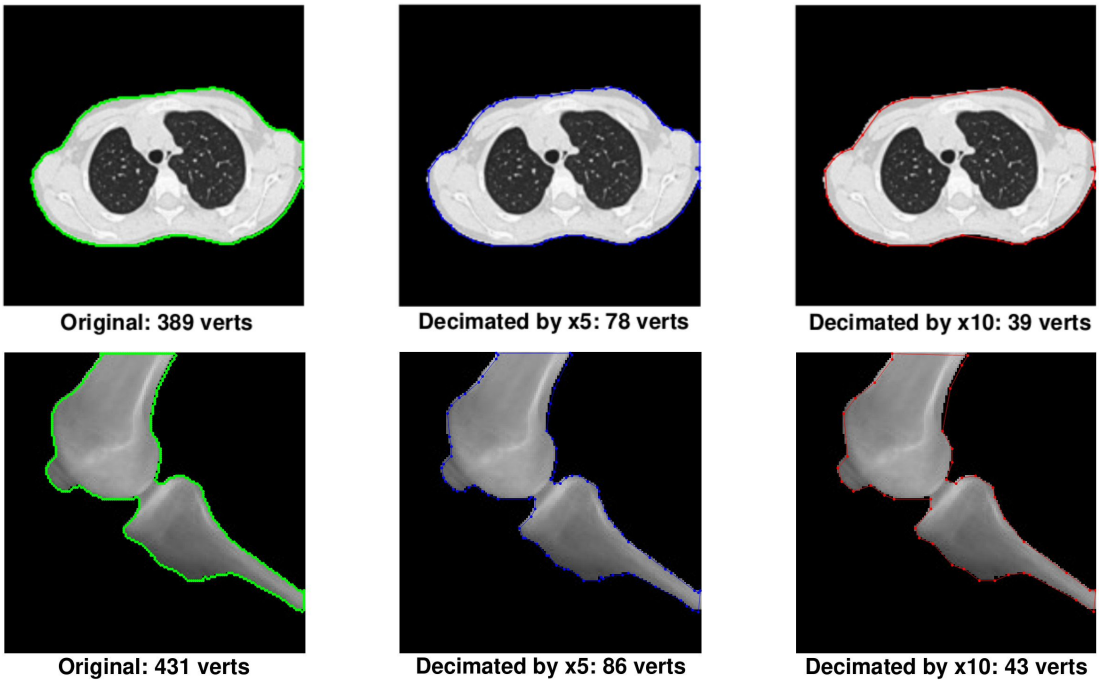

Figure 3.2: Example of dynamic selection with reduced vertex number of segmented RoIs.

The decimated mask of the RoI can be used to locate it in MIs. The representation scheme selects the particular RoI required and disregard the others. How the proposed decimation can capture the desired RoI from the regions segmented is illustrated in Fig. 3.2. Here, the capability of the proposed RoI selection scheme to select different segmented region is shown. At the top row of the figure, the whole outer boundary of the CT chest is selected as RoI and represented, which means that, the scheme

can automatically select any region as RoI if it is segmented. The effectiveness of this representation scheme is verified in the next chapter with more illustrations and technical details.

3.4 Chapter Summary

The proposed automatic selection method discussed in this chapter has captured both the new development of segmentation and representation schemes. The segmentation scheme is developed to detect small changes in image features, and thus, the desired RoI of MI can be effectively separated from RoNI. The proposed ACM-based segmentation can also be tuned to select different RoI shapes and sizes with different image features. After the segmentation, the RoI is represented with a set of reduced number of vertices using the proposed vertex-decimation scheme. The decimation scheme can selectively reduce the vertex-points to represent the RoI. The user thus can get the required number of vertices to represent the RoIs at the cost of relatively less significant RoI or inclusion of RoNI, or both. Moreover, the scheme segment the RoI and also gives the location information with shape. Without hampering the clinical data in the RoI, it can be represented with the minimum information required. The potential of the proposed segmentation and representation schemes are verified in the next chapter.

CHAPTER 4

RESULTS AND DISCUSSION

4.1 Introduction

The performance of the proposed RoI selection method is now examined. As discussed in Chapter 3, the method has two schemes. The first one is a segmentation scheme for the multi-modality MIs. A new scheme is developed that is called weighted relative entropy pre-fitting (WREP) model-based segmentation. The second scheme is to represent the segmented RoIs efficiently. A polygon vertex point reduction scheme is used to develop this representation scheme. The performance of these proposed schemes are now evaluated in this chapter for both the medical and synthetic images with and without the noise and intensity-inhomogeneity. This result and analysis are thus expounded in two sections, namely, '*performance of the proposed segmentation scheme*' in Sec. 4.3 and '*performance of the proposed representation scheme*' in Sec. 4.4.

The segmentation performance of the WREP scheme is evaluated and compared with segmentation schemes based on the LHIF [37] and LPF [38] models, which are two recent and prominent schemes. Additionally, the segmentation performance is evaluated and compared in terms of accuracy, noise withstanding capability, contour evolution speed, and initialization robustness. The segmentation accuracy is determined in reference to the ground-truth images generated by using *ImageJ* application [49]. Noise withstanding capability is tested for additive Gaussian noise with different variance. Initialization robustness is tested to verify the accuracy of the proposed segmentation scheme for the initialized contours at different locations of the image.

Moreover, the performance of the proposed RoI representation scheme is pre-

sented to demonstrate the effectiveness of utilizing less number of vertices for the representation of the segmented RoIs. These results are also illustrated for different test images after reducing the number of vertex points five times and ten times. The amount of information required to represent the shape for different number of vertex points is also compared and analyzed.

4.2 Experimental Settings

Different parameters and performance evaluation parameters are considered and defined below, before presenting the results and analysis of the proposed method in this chapter. The experiments have been conducted in Matlab *R*2016*b* software on a personal computer with 2.6 GHz Intel Core *i*7 processor and 4*GB* physical memory.

4.2.1 Parameters of the ACMs

The parameters of the WREP scheme used in the experiments are summarized in Table. 4.1, and that of the LHIF and LPF models are given in Table. B.1 and Table. B.2. These parameters include S_{kernel}, which is the size of the local window used to calculate local dispersion, and ν and μ, which are the weights of length parameter and level set penalizing term defined with their conventional values. Besides, the level set, ϕ is initialized with -1 inside and $+1$ outside the evolving contour. With $\phi^{n+1} = \phi^n + \Delta t \cdot \Delta\phi^n$, the initial contour evolves iteratively, where n is the number of iteration, and Δt is the time step.

Additionally, a Gaussian kernel of size $(4\sigma+1)\times(4\sigma+1)$ and the standard deviation σ is used to localize the energy functional and to calculate intensity pre-fitting functions in proposed and LPF schemes. The Gaussian kernel of size $(2\sigma+1)\times(2\sigma+1)$ is used in the case of the LHIF scheme. The values of λ_1 and λ_2 in the proposed model and LHIF model controls the first and second terms in (3.2c) and (2.9b), respectively. Here, λ_2 is the weight of the second term in (3.2c) and (2.9b) , which is more

sensitive to variations and should be fixed first. Taking these values into the consideration, the value of λ_2 is ascertained and other constants are properly selected. Here, ε is a function of Δt, while higher values of ε give wider capture range. With these settings, the performance of the proposed segmentation is evaluated and compared with the LHIF and LPF models based segmentation.

4.2.2 Performance evaluation metrics

To compare the accuracy of segmentation, a set of popular evaluation parameters are presented in this section. For test images, we have created a local image database containing MIs of six modalities: X-ray, MRI, CT, DSA, Mammography, and US. A set of respective ground-truth segmented images is also prepared using state-of-the-art ground-truth generating software [49]. Two popular ACM-based segmentation methods [37, 38] have been chosen that showed impressive performance for intensity inhomogeneous and noisy medical and synthetic images. Initialized contour and control parameters are kept the same for individual schemes, to verify their performance in automatic ROI segmentation of multi-modality MIs.

Evaluation procedure broadly can be divided into two types: supervised and unsupervised [50]. Supervised segmentation evaluation procedures use a pre-generated ground-truth image to compare it with the segmented image. It seeks to find out similarities and dissimilarities between segmented and ground truth images. In supervised segmentation evaluation, correctness in the ground truth image influences the possible results. On the other hand, unsupervised methods compare statistics of the segmented image with the original image. These evaluation criteria have no previous information to compare, unlike supervised evaluation criteria. In our work, we have used supervised evaluation criteria to establish the correctness of segmentation schemes.

A number of popular parameters for quantitative performance evaluation are also considered. They are Jaccard Similarity Coefficient (JSC), Dice Similarity Coefficient

Table 4.1: Constant Parameters Used For The Proposed Model-based Segmentation

Test Image	σ	ν	λ_1	λ_2	μ	ε	Δt	S_{kernel}
MRI-brain21	8	.04*255*255	1	0.08	2	6	0.01	3×3
DSA-angiogram10	5	.002*255*255	1	0.05	1	6	0.01	5×5
Mammogram	2	.09*255*255	1	0.02	1	6	0.01	3×3
US-urogenital1	2	.2*255*255	1	0.02	1	6	0.01	3×3
MRI-left-ventricle	12	.02*255*255	1	0.05	1	6	0.005	3×3
MRI-nonuniform	4	.02*255*255	1	0.04	2	6	0.01	3×3
Ct-cardiac	10	.05*255*255	1	0.05	2	6	0.01	5×5
MR-brain	4	.06*255*255	1	0.02	1	6	0.01	3×3
Fluorescence-micrograph	15	.1*255*255	1	0.001	1	6	0.01	3×3
CT-knee1	8	1*255*255	1	0.04	1	6	0.01	3×3
CT-kidney3	10	.09*255*255	1	0.04	1	6	0.005	3×3
CT-kidney7	8	.08*255*255	1	0.1	1	6	0.005	3×3
CT-chest1	8	.08*255*255	1	0.02	1	6	0.01	3×3
X-ray-knee2	8	.01*255*255	1	0.05	1	6	0.005	3×3
X-ray-leg1	4	.02*255*255	1	0.1	1	6	0.005	3×3
Fluoroscopy-bladder2	4	.3*255*255	1	0.03	1	6	0.005	3×3
Fluoroscopy-gastro	1	.03*255*255	1	0.1	1	6	0.005	3×3
DSA-angiogram9	8	.08*255*255	1	0.1	1	6	0.005	3×3
MRI-brain38	5	.2*255*255	1	0.01	1	6	0.005	3×3
MRI-brain39	10	.05*255*255	1	0.004	2	6	0.005	3×3
X-ray-knee1	8	.01*255*255	1	0.005	1	6	0.005	3×3
Fluoroscopy-neck3	1	.008*255*255	1	0.005	1	6	0.05	3×3
Car	6	.06*255*255	1	0.008	1	6	0.003	3×3
CT-heart	5	.03*255*255	1	0.03	2	4	0.001	3×3
F95	4	.002*255*255	1	0.08	0.1	5	0.1	3×3
Angiogram-blood-vessel	3	.005*255*255	1	0.05	1	3	0.01	3×3
Shapes-nonuniform	3	.06*255*255	2	0.1	2	5	0.04	3×3
Shape-inhomogeneous	5	.007*255*255	1	0.1	1	3	0.05	3×3
Star5	3	.0008*255*255	1	2	2	4	0.01	3×3
T-shape	2	.005*255*255	1	0.03	2	3	0.05	7×7
Vessel1	5	.02*255*255	1	0.16	2	4	0.03	3×3
Vessel2	6	.02*255*255	1	0.15	2	6	0.01	7×7
MRI-brain	2	.1*255*255	1	0.05	2	6	0.01	3×3

(DSC), and Modified Hausdorff Distance (MHD). To evaluate the execution speed of the proposed model, the segmentation time and iteration number are used. The performance of the ACM-based segmentation schemes are also evaluated for different initializations and noise.

4.2.2.1 Dice similarity coefficient (DSC)

DSC statistically compares the closeness of two sample sets of data. Given two sets X and Y, DSC is defined in Eq. (4.1). Its value can vary between 0 and 1. It's '0' value means zero overlaps of two sets of data, and '1' value DSC means the data sets completely overlap with each other to be a similar set. For segmentation accuracy computed with respect to the ground truth, a closer value of DSC to 1 means to have more accurate segmentation.

$$D(X,Y) = \frac{2|X \cap Y|}{|X| + |Y|} \tag{4.1}$$

4.2.2.2 Jaccard similarity coefficient (JSC)

It is also called the Jaccard Index (JI). It is used to statistically compare similarity and diversity of two sets of data. It is defined in Eq. (4.2) for two sets of data X and Y. If X and Y both are empty sets, the value of JSC becomes 1. In other cases, JSC value remains within 0 to 1.

$$J(X,Y) = \frac{|X \cap Y|}{|X \cup Y|} \tag{4.2}$$

4.2.2.3 Modified Hausdorff distance (MHD)

It is more powerful than the classical Hausdorff distance (HD) measurement. Hausdorff distance is the maximum distance of a set to the nearest point in the other set. The difference of MHD with HD is it uses average instead of maximum distance. Let us X is our segmented image and Y is our ground truth image, and $d(l,m)$ is the minimum distance of a point l in the set X or segmented image to the point m in set Y. The average distance of all the point l in set X and all the point m in set Y can be calculated using Eq. (4.3a), where $|Y|$ is the total number of elements in Y. The MHD

now can be computed using Eq. (4.3b).

$$h(X,Y) = \frac{1}{|Y|} \sum_{m \in Y} min\{d(l,m) | l \in X\} \tag{4.3a}$$

$$MHD(X,Y) = max(h(X,Y), h(Y,X)) \tag{4.3b}$$

4.3 Performance of the Proposed Segmentation Scheme

4.3.1 Noise and initialization robustness test

The proposed WREP model-based segmentation is designed to be more robust against the varying initialized contours. A segmentation scheme is considered to have this initialization robustness if the scheme can accurately segment for the initialized contours with different locations and sizes. The performance of the proposed segmentation model is first evaluated for initialization robustness and compared with the LPF model and LHIF models for the same initialization. This performance for both the intensity inhomogeneous and noisy images is illustrated in Fig. 4.1. Here, the result comparison for proposed (*left column*), LPF [38] (*middle column*), and LHIF [37] (*right column*) models is shown. It is observed that the proposed scheme can successfully segment for both the cases. The LPF model-based scheme can also segment the images. Unlike the proposed and LPF model, the LHIF model, however, generates wrong contour evolution for most cases of initialization in Fig. 4.1.

Additionally, the noise withstanding capability of the proposed scheme is evaluated and verified over the segmentation schemes based on the LHIF and LPF models. An example with a few test images is illustrated in Fig. 4.2, where the Gaussian noise of standard deviation 5 (left column), 10 (middle column), and 15 (right column) are used. It is observed that the segmentation schemes based on the proposed model and LPF model generate a successful result, but the LHIF model-based scheme generates wrong segmentation results for the noisy images.

The results of the initialization robustness test and noise withstanding capability

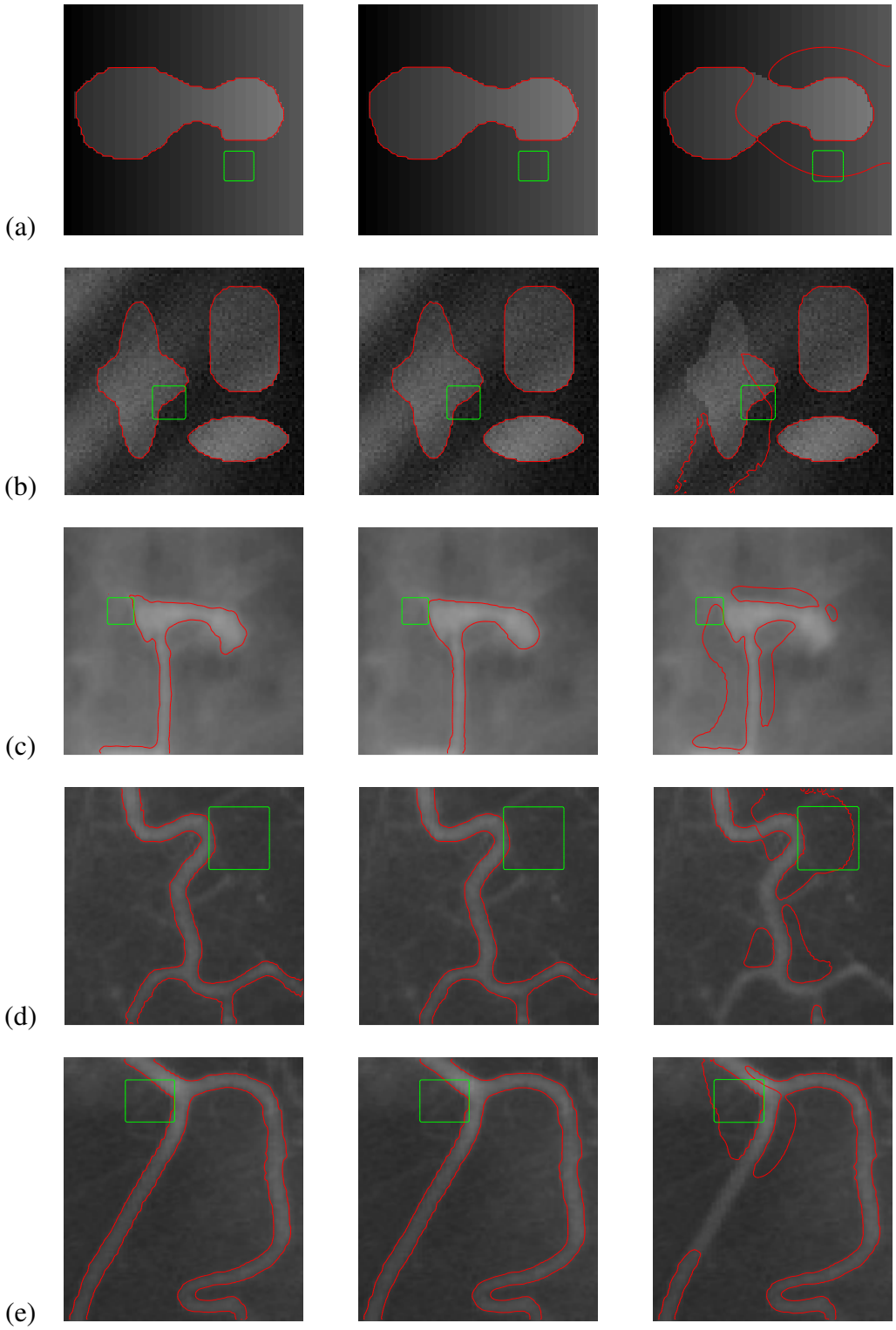

Figure 4.1: Initialization robustness against the intensity inhomogeneity and noise for: (a) shape-nonuniform, (b) shapes-inhomogeneous, (c) shape-low-contrast, (d) vessel11 (nonuniform), and (e) vessel12 (low contrast).

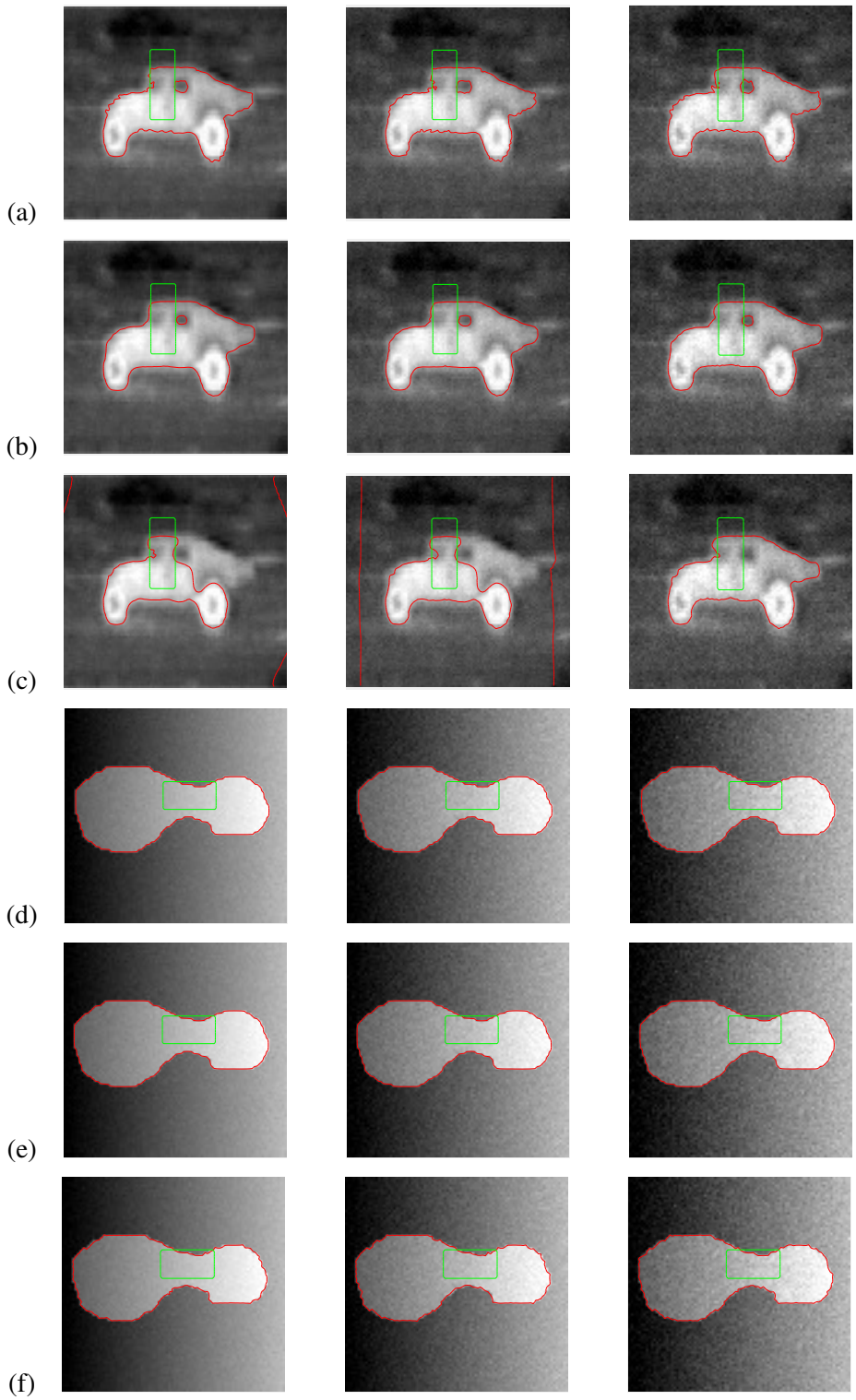

Figure 4.2: Segmentation robustness against the Gaussian noise for the *car* and *shape-inhomogeneous* images: (a,d) proposed, (b,e) LPF [38] and (c,f) LHIF [37].

test suggest that the proposed WREP model and LPF model both would work reasonably better than the LHIF model. Noise withstanding capability of the proposed model is improved by using pre-fitting functions in the energy equation. Thus, the accuracy in the generated contour of the proposed scheme is more consistent. Besides, the contours of the proposed scheme remain smoother due to scaling with edge mapped image constructed with the local dispersion.

4.3.2 Subjective assessment of the segmentation accuracy

Generally, accuracy is a key performance criterion of a segmentation scheme. Subjective assessment of the segmentation accuracy has already been partially verified for the initialization robustness in the previous section. The performance of the proposed segmentation scheme is now presented and compared with the schemes based on the LPF and LHIF models for different modality MIs and synthetic images. This performance is analyzed with the example of the segmented images in Fig. 4.3, Fig. 4.4, and Fig. 4.5.Here from Fig. 4.3 to Fig. 4.5, result of proposed model is in *left column*, LPF model [38] is in *middle column* and LHIF model [37] is in *right column*. Additional results for more MIs are also included in the Appendix. B.2.

Both Fig. 4.3, and Fig. 4.4 demonstrates that the proposed WREP model-based scheme can segment the RoI accurately for different modality MIs. Particularly, the segmentation schemes based on the proposed and LPF models can segment the selected RoI successfully for the computed tomography (CT) images of cardiac, chest, and knee in Fig. 4.3. Unlike these schemes, the LHIF model-based segmentation scheme, however, produces wrong contours. In contrast, for the DSA blood vessel image, a few trivial edge-leakages are seen for the proposed and LPF models, which were absent in the result of the LHIF-based scheme. The proposed and LPF schemes, however, work better than the LHIF model for the fluoroscopic bladder image.

Similar results of the proposed segmentation scheme are also evident for the X-ray

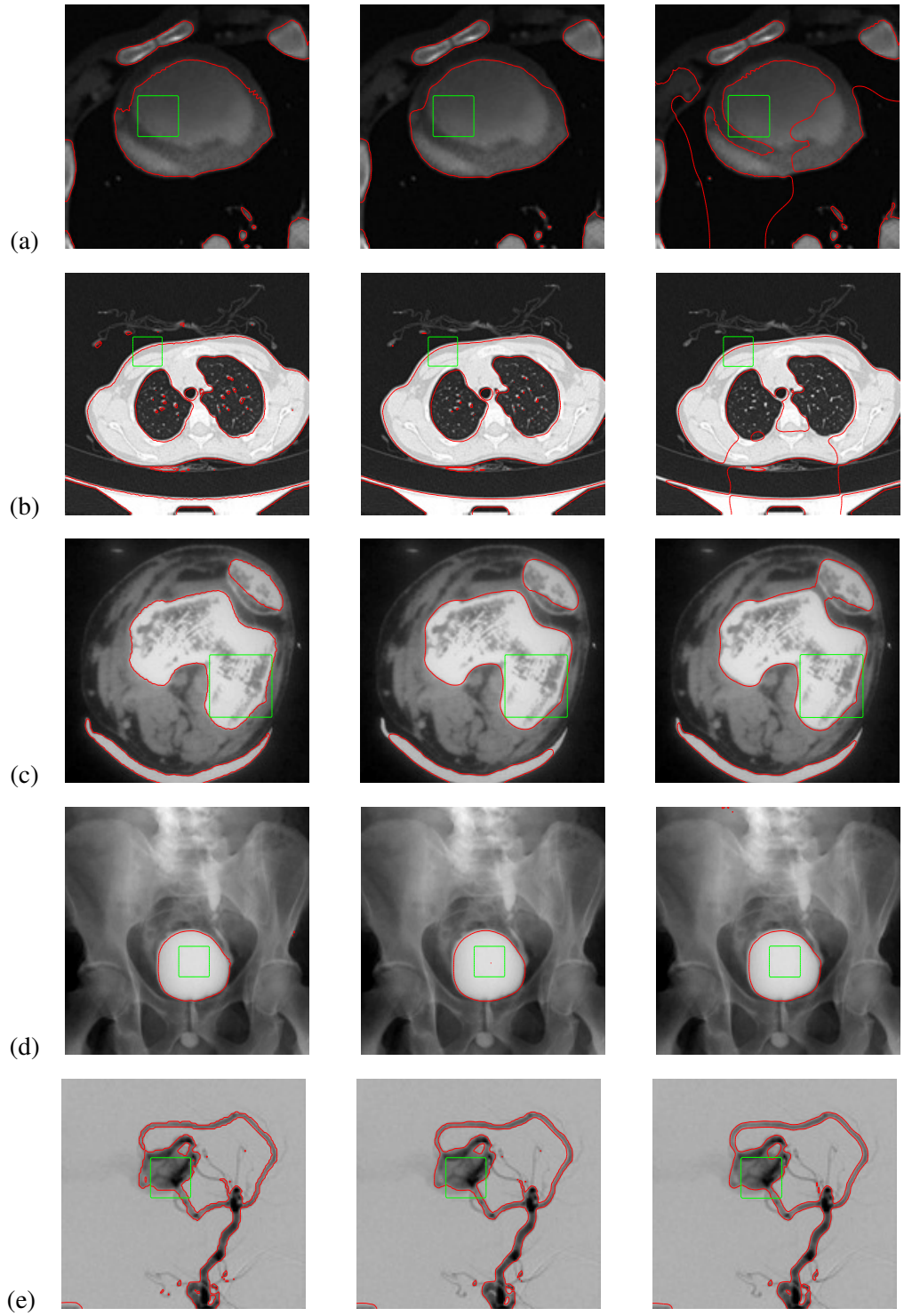

Figure 4.3: Segmentation results of the schemes for: (a) CT image (cardiac), (b) CT image (chest), (c) CT image (knee), (d) Fluoroscopic image (bladder), and (e) DSA image (blood-vessel).

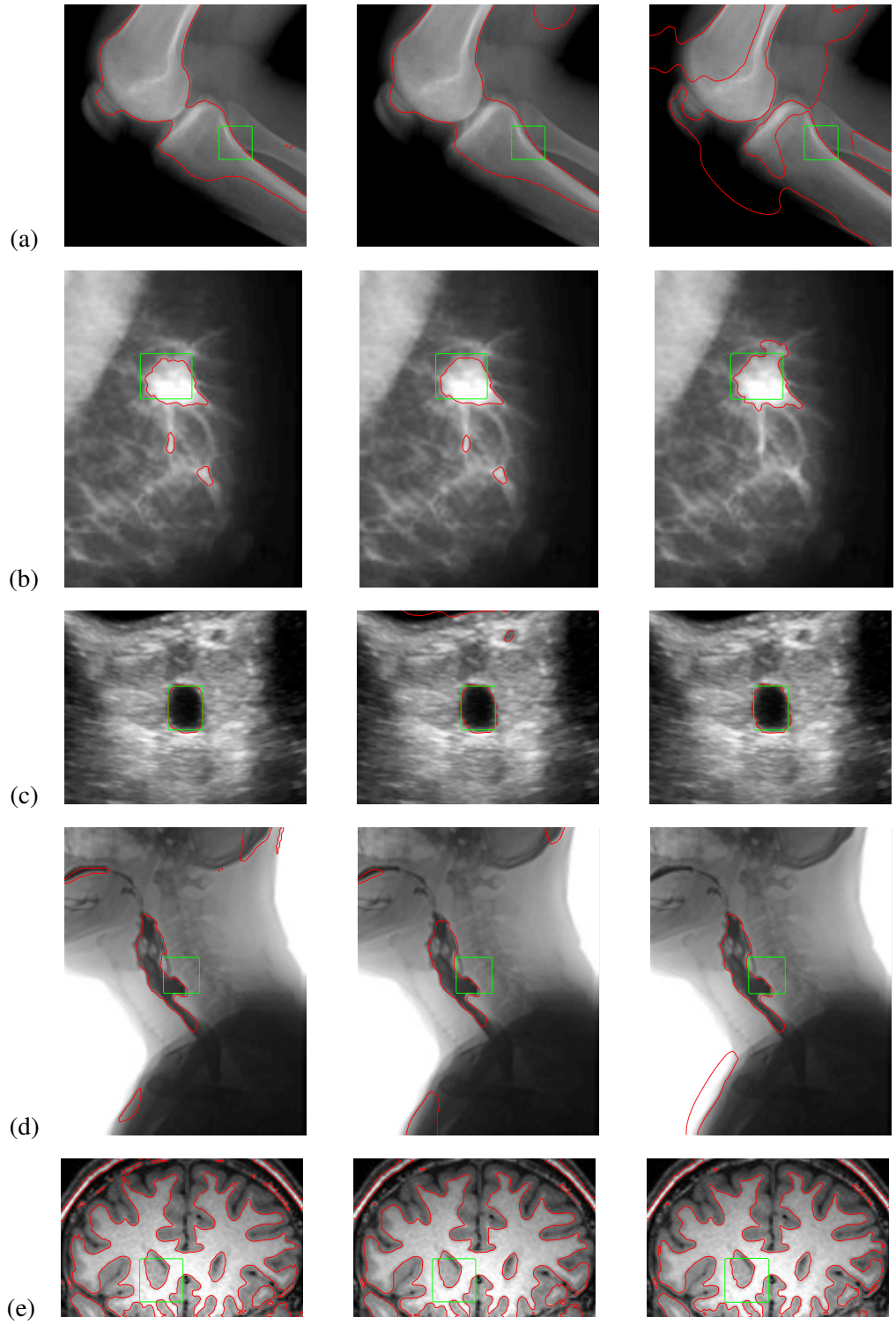

Figure 4.4: Segmentation results of the schemes for: (a) X-ray image (knee1), (b) Mammography image (breast), (c) US image (urogenital), (d) Fluoroscopic image (neck), and (e) MRI (brain).

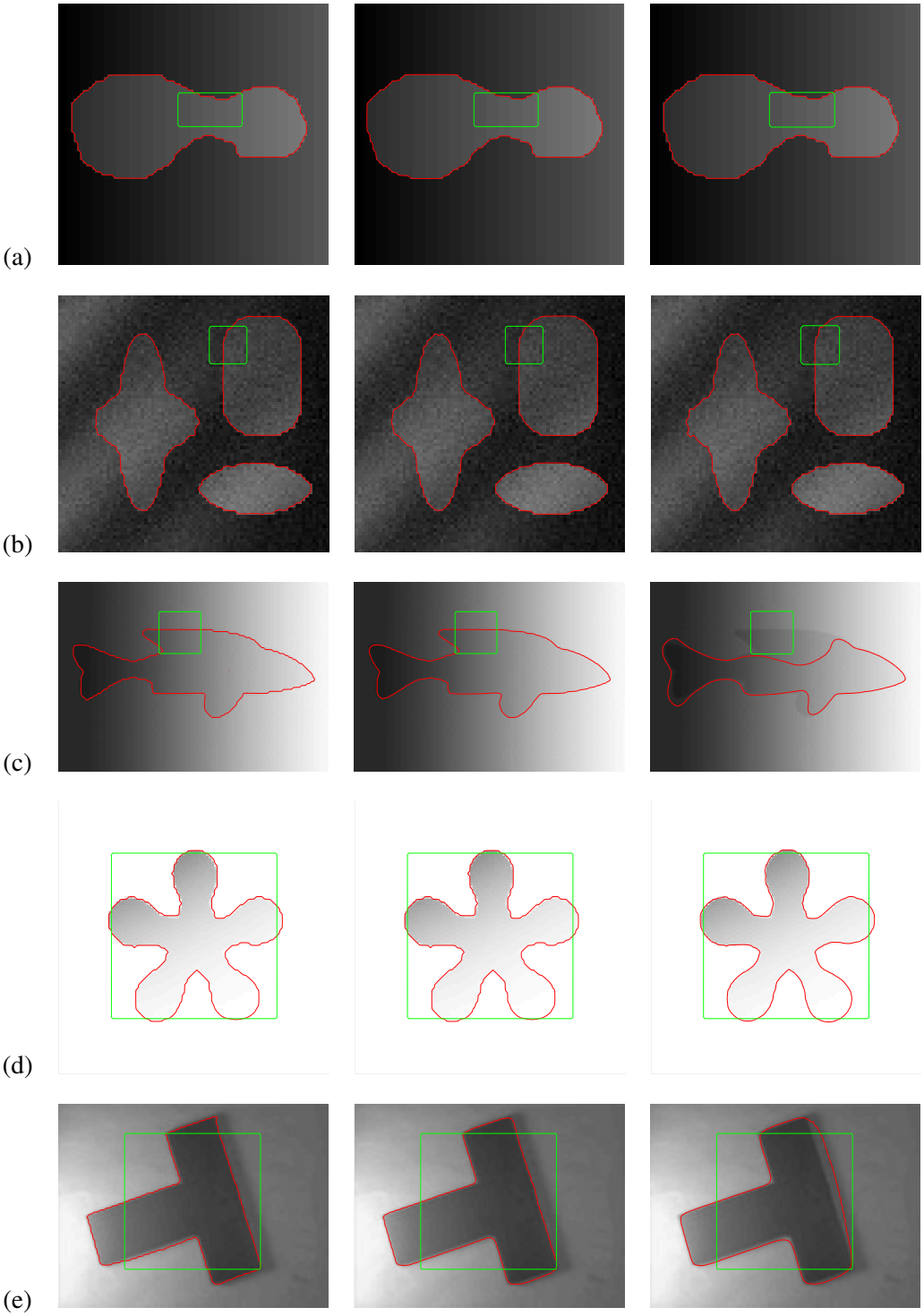

Figure 4.5: Segmentation results of the schemes for different level of noise and intensity inhomogeneity in the synthetic images: (a) shape-inhomogeneous, (b) shapes-nonuniform, (c) F95-inhomogeneous, (d) Star5, and (e) T-shape.

Table 4.2: Comparison of Segmentation Accuracy

Test Image	WREP (proposed)			LPF [38]			LHIF [37]		
	JI	**DSC**	**MHD**	**JI**	**DSC**	**MHD**	**JI**	**DSC**	**MHD**
Shapes-nonuniform	0.9844	0.9921	0.3209	0.9834	0.9916	0.3609	0.9782	0.989	0.0218
Vessel1	0.8251	0.9042	1.0488	0.8466	0.9169	0.8531	0.8459	0.9165	0.9179
Vessel2	0.8587	0.924	1.3055	0.8601	0.9248	1.3274	0.7973	0.8872	1.7417
Shape-inhomogeneous	1	1	0	1	1	0	0.9854	0.9926	0.2381
MRI-brain	0.8937	0.9439	0.794	0.8658	0.9281	0.9442	0.8662	0.9283	0.9403
CT-kidney7	0.9652	0.9823	0.3693	0.956	0.9775	0.3577	0.9412	0.9697	0.5097
CT-knee1	0.9324	0.965	1.1551	0.897	0.9457	1.4438	0.891	0.9424	1.4818
DSA-angiogram9	0.9226	0.9598	0.5976	0.9293	0.9633	0.5204	0.8865	0.9398	0.7398
Fluoroscopy-bladder2	0.9855	0.9927	0.074	0.9871	0.9935	0.0722	0.9844	0.9922	0.0779
X-ray-knee2	0.8823	0.9375	0.7268	0.793	0.8846	1.23	0.7007	0.824	1.7172

image of the knee, US image of urogenital, and mammography image of the breast in Fig. 4.4. Particularly, the proposed scheme can accurately identify internal bone structure for all the X-ray images. The LPF model-based scheme also works with similar accuracy, but that scheme occasionally fails to identify parts of the bone structure in the X-ray image of the knee. For the MRI brain images, the proposed model can also identify the selected RoIs with the internal blobs efficiently. Besides, the LHIF model-based scheme generates wrong contours in most of the cases, except for the mammography image of the breast, where that model exhibits slightly better result with no edge leakage like the proposed and LPF models-based schemes.

Additionally, Fig. 4.5 illustrates the segmentation performance of these schemes for the standard synthetic images with different levels of noise and intensity inhomogeneity. As already observed for the MIs, the proposed and LPF schemes are also found to work better than the LHIF scheme. Considering these overall subjective observations, the proposed model demonstrates reasonably better accuracy than the LPF and LHIF models.

Table 4.3: Average Segmentation Time and Iteratation Comparison

Image Modality	WREP (Proposed)		LPF [38]		LBIF [37]	
	Time (*s*)	**Iteration**	**Time (*s*)**	**Iteration**	**Time (*s*)**	**Iteration**
CT	2.99	167	3.20	188	8.16	262
DSA	1.48	37	1.53	33	3.32	293
Fluoroscopy	2.79	86	3.17	168	5.87	213
MRI	2.71	120	3.06	139	5.22	264
X-ray	3.42	190	3.39	213	6.11	283
Synthetic	1.30	92	1.50	149	3.89	344
Other MIs	2.46	39	3.34	61	3.26	96

4.3.3 Objective assessment of the segmentation accuracy

The objective assessment is also carried out to verify the segmentation accuracy of the proposed scheme quantitatively. The segmented test images are compared with ground-truth images. The result of proposed model-based segmentation is compared with LPF and LHIF models using popular segmentation evaluation parameters like Jaccard Index (JI), Dice Similarity Coefficient (DSC), and Modified Hausdorff Distance (MHD). This comparison is presented in Table. 4.2. Generally, the result of the LPF model and the proposed model is very close. The average JI value for the proposed model is of about 0.92, which is 0.91 for the LPF model and 0.89 for the LHIF model. In the case of DSC, the proposed model has an average of 0.96, where the LPF has this value of 0.95, and the LHIF has this value of 0.94. Moreover, a smaller value of MHD is desirable due to its closeness to zero value represents a perfect segmentation for a given ground-truth. The proposed segmentation scheme has scored an average MHD of 0.64, where the LPF model has this value of 0.71, and the LHIF model has scored of about 0.84. These quantitative values for the performance parameters (*i.e.*, JI, DSC, and MHD) suggest that the proposed WREP model-based segmentation outperforms the LPF and LHIF models.

Table 4.4: Comparison of Execution Time and Iteration Number

Test Image	WREP (proposed)		LPF [38]		LHIF [37]	
	Time	**Iteration**	**Time**	**Iteration**	**Time**	**Iteration**
MRI-brain21	1.552	10	2.024	10	3.440	50
DSA-angiogram10	1.982	50	2.130	50	2.684	80
Mammogram	1.255	50	1.102	50	0.652	40
US-urogenital1	7.548	50	10.83	120	10.15	120
MRI-left-ventricle	4.740	200	5.268	150	3.678	350
MRI-non-uniform	2.288	150	2.520	200	8.528	300
CT-cardiac2	4.842	400	3.524	150	7.093	400
MR-brain	1.848	50	2.276	100	3.736	150
Fluorescence-nucleus	4.341	45	4.499	70	7.615	200
CT-knee1	4.799	325	5.087	385	21.13	300
CT-kidney3	1.376	10	1.681	30	1.433	120
CT-kidney7	1.679	30	1.905	30	5.133	200
CT-chest1	2.567	35	3.134	30	10.04	400
X-ray-knee2	2.690	70	2.352	40	9.357	300
X-ray-leg1	2.219	100	2.805	250	3.933	200
Fluoroscopy-bladder2	1.874	50	2.541	200	2.397	100
Fluoroscopy-gastrointestinal5	2.132	100	2.404	150	8.721	200
DSA-angiogram9	1.880	40	1.930	20	1.843	150
MRI-brain38	2.753	100	2.993	100	5.048	450
MRI-brain39	4.598	280	5.095	350	9.851	350
X-ray-knee1	5.344	400	5.012	350	5.047	350
Fluoroscopy-neck3	2.817	150	3.241	250	4.734	350
Car	1.758	90	1.976	180	2.975	400
CT-heart	2.692	200	3.895	500	4.114	150
F95	1.328	53	1.765	120	9.888	950
Angiogram-blood-vessel	0.567	20	0.527	30	5.428	650
Shapes-nonuniform	0.469	30	0.868	50	0.687	65
Shape-inhomogeneous	0.452	20	0.557	45	0.678	50
Star5	2.476	300	2.351	400	1.754	200
T-shape	1.307	60	1.495	100	7.352	400
Vessel11	0.526	30	0.531	20	1.344	150
Vessel12	0.493	25	0.889	55	0.906	75
MRI-brain	1.159	50	1.219	60	2.246	200

4.3.4 Segmentation time and iteration comparison

The execution time and iteration number of the proposed scheme have also been recorded. Table 4.3 presents the modality-wise average iteration time in seconds and iteration number to segment different test images for the proposed, LPF, and LHIF models. Complete results are given in Table 4.4. The average time and iteration in Table 4.3 show that the CT, X-ray, and MRI require a relatively high number of iteration and segmentation time. For these modality MIs, the proposed WREP-based segmentation requires the lowest number of iterations and segmentation time compared to the other schemes. It may also be noted that the LPF -based scheme has relatively closer segmentation time and iterations, while the LHIF-based scheme has a far higher requirement. A similar trend of improvement of the proposed scheme also exists for the synthetic and other modality MIs. These observations can be summarized to conclude that the proposed model can offer faster segmentation due to the effective approximation of the Gaussian kernels and the use of relative entropy based energy functional.

4.4 Performance of the Proposed RoI Representation Scheme

The results of the proposed RoI representation scheme after segmentation are now expounded. Once the segmentation is done, boundary points of the RoI are calculated, and then the proposed decimation scheme is applied to the RoI boundary-points that are called here the vertex points. The shape of RoI after reducing the number of these vertex points for 5 times and 10 times from the original vertex points can still represent the shape accurately. These representations are illustrated in Fig. 4.6, and Fig. 4.7 for subjective analysis. Additional results are also given in the Appendix (see Fig. B.3 and Fig. B.4).

Effective representation of a segmented RoI can be ensured with the decimation parameter. For example, the segmented RoIs of MRI and CT images are illustrated

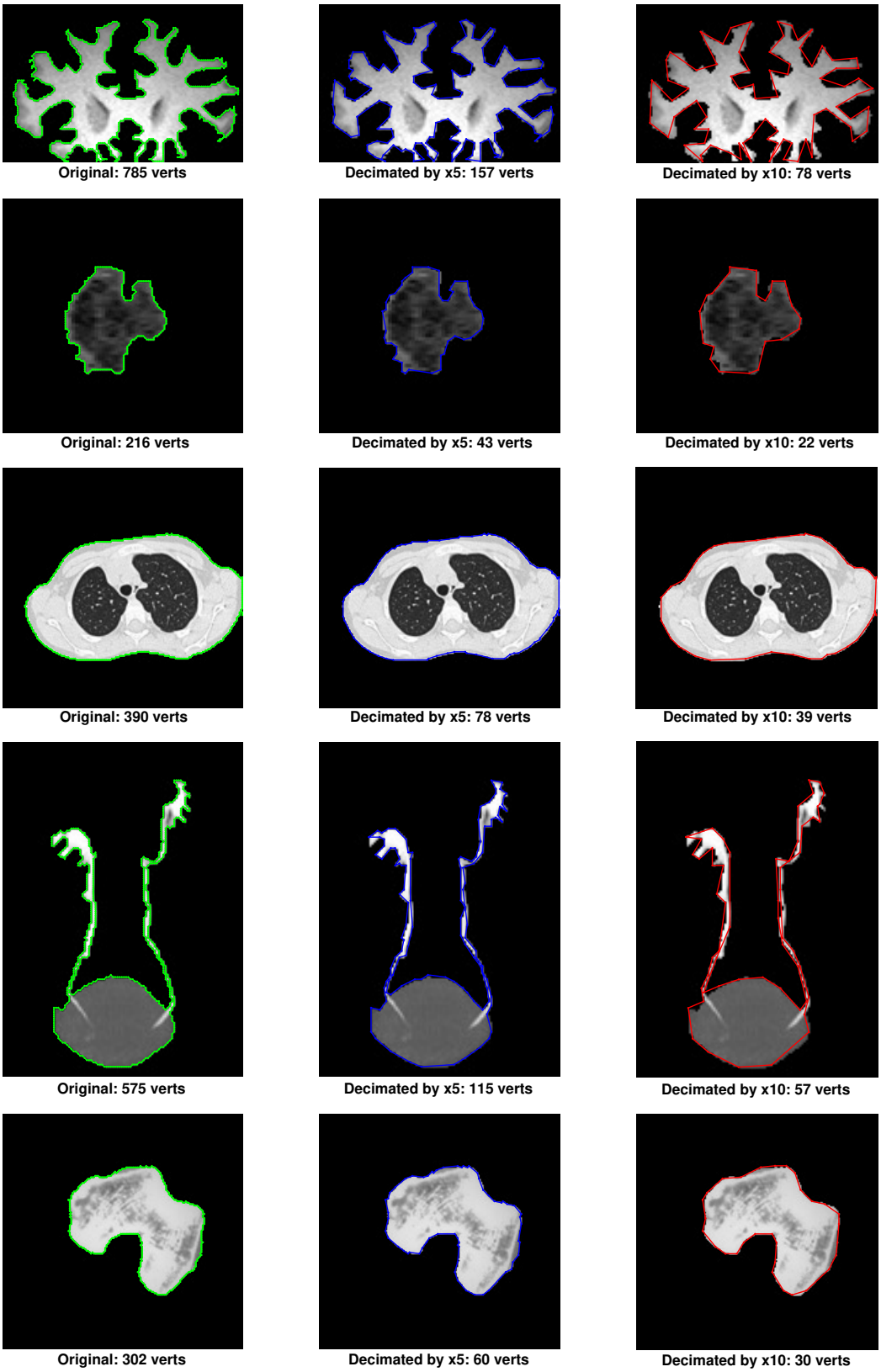

Figure 4.6: Vertex number decimation of segmented RoI vertex points in MRI-brain (from *top*, 1^{st} row), MRI-left-ventricle (2^{nd} row), CT-chest (3^{rd} row), CT-kidney (4^{th} row) and CT-knee (5^{th} row).

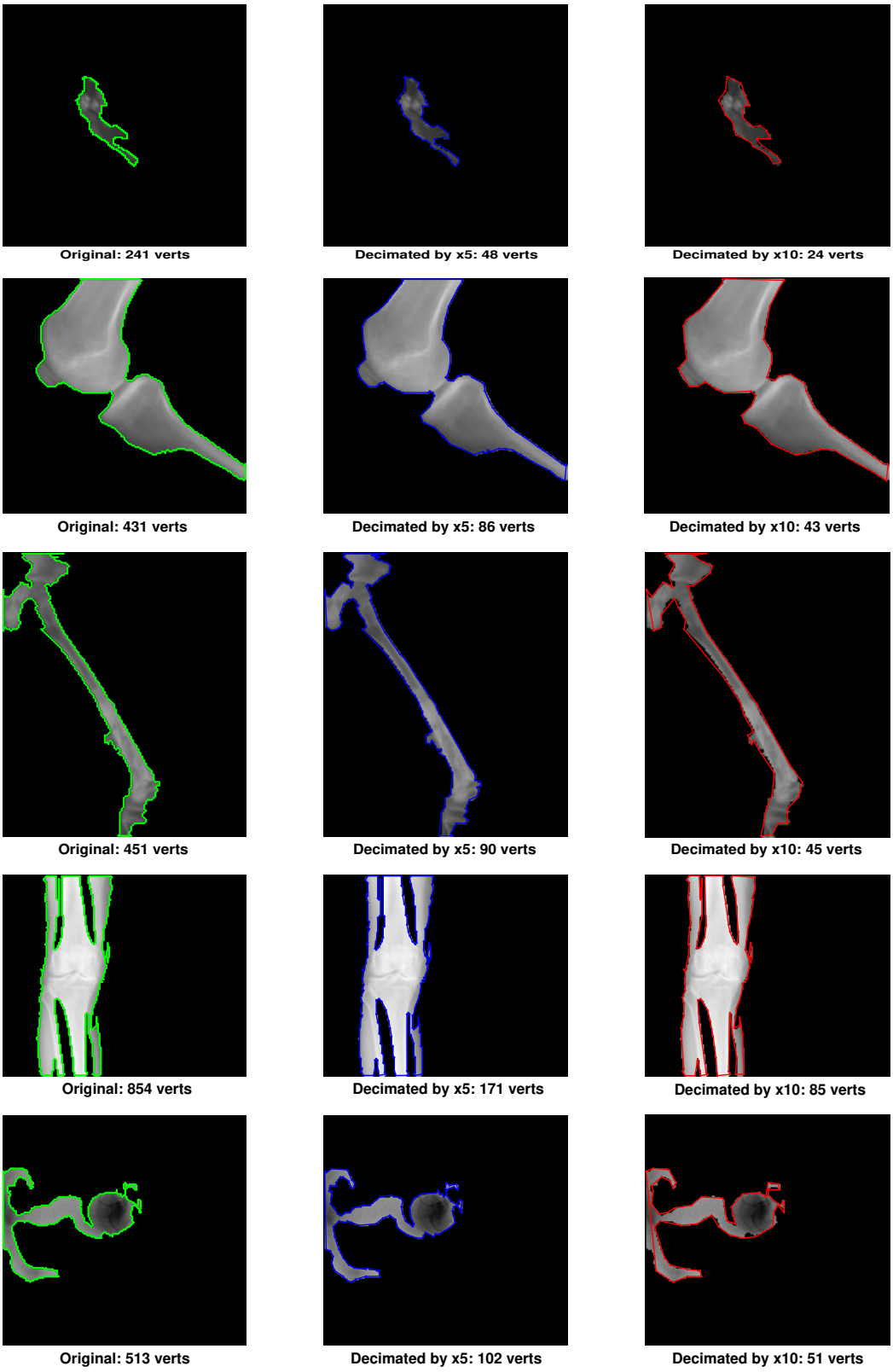

Figure 4.7: Vertex number decimation of segmented RoI vertex points in Fluoroscopy-neck(from *top*, 1^{st} row), X-ray-knee1 (2^{nd} row), X-ray-knee2 (3^{rd} row), X-ray-leg (4^{th} row) and DSA-vessel (5^{th} row).

Table 4.5: Reduction of Bit Requirement for RoI Representation

Test Image	Reduction in Bit requirement					
	Original	**Bit**	5× **Decimated**	**Bit**	10× **Decimated**	**Bit**
MRI_brain	80	1280	16	256	8	128
DSA-angiogram10	513	8208	102	1632	51	816
Mammography breast	71	1136	14	224	7	112
US-urogenital1	207	3312	41	656	21	336
MR-leftventricle	216	3456	43	688	22	352
MR-Cardiact2	215	3440	43	688	21	336
MR-brain	785	12560	157	2512	78	1248
Fluorescence-micrograph	187	2992	37	592	19	304
CT-knee1	302	4832	60	960	30	480
CT-kidney3	283	4528	56	896	28	448
CT-kidney7	575	9200	115	1840	57	912
CT-chest1	390	6240	78	1248	39	624
X-ray-knee2	451	7216	90	1440	45	720
X-ray-leg1	780	12480	156	2496	78	1248
Fluoroscopy-bladder2	143	2288	28	448	14	224
Fluoroscopy-gastro	391	6256	78	1248	39	624
MR-brain38	154	2464	31	496	15	240
MR-brain21	154	2464	31	496	15	240
X-ray-knee1	431	6896	86	1376	43	688
Fluoroscopy-neck3	241	3856	48	768	24	384

in Fig. 4.6 with their original vertex numbers. With the 5 and 10 times decimation, the original vertex number of 785 is reduced to 157 and 78 for the MR-brain image (first row in Fig. 4.6). Such a dramatic efficiency in RoI representation without much compromise of their original shape is also achieved for the images in both Fig. 4.6. and Fig. 4.7. It may also be noted that more reduction of the vertex-numbers can be achieved at a higher time decimation, if a slight adjustment in the original segmented RoI's shape is acceptable.

A lesser number of vertex would essentially reduce the requirement of side

information in region-based applications. Each vertex is defined in bits, and the side information is calculated from the total number of vertices. Table. 4.5 summarizes the bits required for the decimated vertex numbers for the segmented RoIs in different MIs. It is seen from the table that for the MR_brain image, a total of 80 vertices of the originally segmented RoI requires 1280 bits, which can be reduced to 256 and 128 bits with 5 and 10 times decimation, respectively. With another example of the DSA image of the blood vessel, it can be seen that the total 513 vertices of the originally segmented RoI require 8208 bits, which can be reduced to 1632 and 816 bits with 5 and 10 times decimation, respectively. These reductions mean that, with the 5 and 10 times decimation, the bit-requirements can be reduced by about 80% and 90%, respectively A similar trend of lower bit requirement also exists for the other MIs. The proposed selection scheme thus can efficiently and selectively represent the RoI without any noticeable change in its basic shape.

4.5 Chapter Summary

The effectiveness and efficiency of the proposed RoI selection method are demonstrated in this chapter by analyzing the performance of its underlying schemes: the newly developed RoI-segmentation and RoI-representation schemes. The performance of the developed ACM-based segmentation scheme, which is called the WREP model-based segmentation, is compared with the other recent schemes in terms of accuracy, execution speed, initialization robustness, and noise withstanding capability. The WREP-based segmentation scheme is found more accurate, faster, and more robust against the initialized contours and noise than the LPF and LHIF-based schemes. Additionally, the presented RoI representation scheme has also demonstrated its efficiency in capturing the segmented shape of RoI without any noticeable loss of clinically important information. With a selective decimation, the RoI can be represented with 80%

or more less number of bits. The proposed RoI selection method thus combines the effectiveness and efficiency of the developed segmentation and selection schemes.

CHAPTER 5

CONCLUSIONS AND FUTURE WORKS

5.1 Conclusions

The aim of the presented research in this thesis is to develop an efficient and automatic RoI selection method for region-based MI processing applications. In region-based MI processing and its applications, RoI of the MI is kept un-touched to protect crucial clinical information from distortion. A key prior-requirement of region-based MI processing is to select, separate, and preserve the RoI. This requirement can be achieved with the segmentation of RoI followed by its representation with location information saved as side information.

However, the region-based processing has not been paid due importance for efficient segmentation and representation of RoIs. Related literature finds no significant effort made to improve the RoI selection method leaving opportunities for its development. Most of the literature used manual selection of RoI by a radiologist using computer aided drawing tool, which is less-efficient, time-consuming, and cumbersome for a large number of images. The use of the basic segmentation schemes like thresholding, edge detection, or clustering can also be tracked. Since the MI segmentation is a difficult task due to the different shape, size, location and intensity profile of the RoIs in different modalities, those basic schemes are usually incapable of segmenting the RoIs. The presence of noise and intensity inhomogeneity makes this task even more challenging. So, a need for a suitable segmentation scheme is identified to increase the efficiency of the automatic selection process of RoI.

Additionally, as another part of the RoI selection method, existing representation schemes with basic shapes like rectangle, circle, ellipse, or combination of these shapes

remained inefficient and incapable to accommodate complex RoIs in MIs. For higher accuracy, RoIs are to be represented with their original shape, which may eventually require a significantly higher number of vertex points in the RoI contour. An efficient reduction of the number of vertex points without compromising clinical data in RoI is, therefore, another milestone for the envisaged RoI selection method.

An original contribution has thus been made to the development of a new RoI selection method for region-based MI applications. A new ACM-based segmentation scheme has been developed, which is called the WREP model-based segmentation scheme. ACM-based segmentation schemes can consider changes in multiple image features simultaneously, making them robust against the noise, intensity inhomogeneity, low contrast, poorly defined or broken edge, and complex background. In the WREP-based scheme, two new constructions of local images were proposed using local intensity averages calculated locally without Gaussian convolution to expedite the contour evolution. Its noise tolerance, initialization robustness, and time efficiency are also improved by fitting the local images to relative entropy based energy functional. Besides, the energy functional is scaled with a local dispersion based edge mapped image for accuracy in boundary detection and smoother contour generation. On the other hand, unlike the basic shape based schemes, an improved representation scheme is proposed utilizing a vertex decimation technique to efficiently locate and define the segmented RoIs.

The performance of the proposed RoI selection method has been verified by analyzing the performance of the newly developed segmentation and selection schemes. For the MIs of all the commonly used modalities and synthetic images, both with and without noise, intensity inhomogeneity, and low contrast, the segmentation accuracy, speed, and robustness of the segmentation scheme have been analyzed. Compared to the promising and recently reported schemes, the WREP-based segmentation scheme is found more accurate, faster, and more robust against the initialized contours and

noise. Additionally, the presented RoI representation scheme has also demonstrated its efficiency in capturing the segmented shape of RoI without any noticeable loss of clinically important information. With a selective decimation, the RoI can be represented with the 80% or more less number of bits. The proposed RoI selection method thus combines the effectiveness and efficiency of the developed segmentation and selection schemes and can be promising for the timely region-based applications of MIs.

5.2 Summary of Major Contributions

For the presented RoI selection method for region-based MI applications, this thesis introduces a number of original developments. Some of the research contributions are already published in reputed international conferences and some are in the process of publication in future. The notable contributions of the work are given below.

(*i*) Developed an efficient ACM based RoI segmentation scheme for multi-modality medical images.

(*ii*) Generated data set of multi-modality MIs with varying location, size, shape and intensity profile of RoI.

(*iii*) Generated data set of ground truth images by using state of the art segmentation software.

(*iv*) Proposed polygon reduction method to reduce the number of vertices and information required to represent RoI.

(*v*) Integrated the RoI segmentation and representation to design an efficient and automatic RoI selection technique for region-based processing in multi-modality MIs.

5.3 Future Works

Some probable directions of future work have also been identified. A further effort can be made in the development of recent and promising region-based MI applications like the data hiding schemes using the proposed RoI selection method. As the accuracy of the proposed RoI selection method highly depends on the performance of segmentation, a more efficient segmentation scheme may be developed by considering the recent spatial statistics and their measures. The potential of the developed segmentation scheme may be extended and verified for the color image and higher dimensional MIs. A more efficient shape reduction scheme may be also developed and used to improve the capability of RoI representation.

LIST OF PUBLICATIONS

Journal Paper:

(i) **C. M. A. Rahman,** and H. Nyeem, "Entropy Scalable Fitting Model for Intensity Inhomogeneous and Noisy Image Segmentation," *IET Image Processing*, to be submitted. (With supervisor)

Conference Papers:

(i) **C. M. A. Rahman,** and H. Nyeem, "RONI Segmentation for Medical Image Watermarking," in *Proc. 3rd ICEEICT'16*, Dhaka, Bangladesh, IEEE, 2016, pp. 1-6.

(ii) **C. M. A. Rahman,** and H. Nyeem, "Developing Poly-Mask for Automatic ROI Selection of Medical Images," in *Proc. ICEEE'17*, Rajshahi, Bangladesh, IEEE, 2017, pp. 1-4.

(iii) **C. M. A. Rahman,** and H. Nyeem, "Active Contour based Segmentation of ROIs in Medical Images," in *Proc. 2nd ECCE'19*, Cox's Bazar, Bangladesh, IEEE, 2019, pp. 1-6.

(iv) **C. M. A. Rahman,** and H. Nyeem, "A New Weighted Relative Entropy Pre-Fitting for Active Contour based Image Segmentation," in *Proc. IEEE SPICSCON'19*, Dhaka, Bangladesh, IEEE, 2019. (Received best paper award)

(v) **C. M. A. Rahman,** and H. Nyeem, "Relative Entropy Pre-Fitting Model for Noisy and Intensity Inhomogeneous Image Segmentation," in *Proc. 3rd ICTP 2019*, Dhaka, Bangladesh, IEEE, 2019. (Accepted)

BIBLIOGRAPHY

[1] R. Pandey, A. K. Singh, B. Kumar, and A. Mohan, "Iris based secure nroi multiple eye image watermarking for teleophthalmology," *Multimedia Tools and Applications*, vol. 75, no. 22, pp. 14 381–14 397, 2016.

[2] G. Coatrieux, J. Montagner, H. Huang, and C. Roux, "Mixed reversible and roni watermarking for medical image reliability protection," in *Proc. 29th IEEE EMBS*. IEEE, 2007, pp. 5653–5656.

[3] N. A. Memon and S. Gilani, "Nroi watermarking of medical images for content authentication," in *Proc. 13th IEEE INMIC*. IEEE, 2008, pp. 106–110.

[4] H. Nyeem, W. Boles, and C. Boyd, "Digital image watermarking: its formal model, fundamental properties and possible attacks," *EURASIP Journal on Advances in Signal Processing*, vol. 2014, no. 1, p. 135, 2014.

[5] V. Fotopoulos, M. L. Stavrinou, and A. N. Skodras, "Medical image authentication and self-correction through an adaptive reversible watermarking technique," in *Proc. 8th IEEE Int. Conf. BIBE*. IEEE, 2008, pp. 1–5.

[6] H. Nyeem, W. Boles, and C. Boyd, "A review of medical image watermarking requirements for teleradiology," *Journal of digital imaging*, vol. 26, no. 2, pp. 326–343, 2013.

[7] X. Guo and T.-g. Zhuang, "A region-based lossless watermarking scheme for enhancing security of medical data," *Journal of Digital Imaging*, vol. 22, no. 1, pp. 53–64, 2009.

[8] H. Al-Dmour and A. Al-Ani, "A medical image steganography method based on integer wavelet transform and overlapping edge detection," in *International Conference on Neural Information Processing*. Springer, 2015, pp. 436–444.

[9] S. Zhang, T. Gao, and L. Gao, "A novel encryption frame for medical image with watermark based on hyperchaotic system," *Mathematical Problems in Engineering*, vol. 2014, 2014.

[10] H. Nyeem, W. Boles, and C. Boyd, "Content-independent embedding scheme for multimodal medical image watermarking," *Biomedical engineering online*, vol. 14, no. 1, p. 7, 2015.

[11] A. Al-Haj and A. Amer, "Secured telemedicine using region-based watermarking with tamper localization," *Journal of Digital Imaging*, vol. 27, no. 6, pp. 737–750, 2014.

[12] X. Guo and T.-g. Zhuang, "A region-based lossless watermarking scheme for enhancing security of medical data," *Journal of digital imaging*, vol. 22, no. 1, pp. 53–64, 2009.

[13] P. Tsai, Y.-C. Hu, and H.-L. Yeh, "Reversible image hiding scheme using predictive coding and histogram shifting," *Signal Processing*, vol. 89, no. 6, pp. 1129–1143, 2009.

[14] H. Nyeem, "A digital watermarking framework with application to medical image security," Ph.D. dissertation, Queensland University of Technology, 2014.

[15] H. Nyeem, W. Boles, and C. Boyd, "Utilizing least significant bit-planes of RONI pixels for medical image watermarking," in *Proc. DICTA'13*. Piscataway: IEEE, 2013, pp. 1–8.

[16] J. Fridrich, M. Goljan, and R. Du, "Lossless data embedding for all image formats," in *Security and Watermarking of Multimedia Contents IV*, vol. 4675. International Society for Optics and Photonics, 2002, pp. 572–583.

[17] J. Tian, "Reversible data embedding using a difference expansion," *IEEE Transactions on Circuits and Systems for Video Technology*, vol. 13, no. 8, pp. 890–896, 2003.

[18] Z. Ni, Y.-Q. Shi, N. Ansari, and W. Su, "Reversible data hiding," *IEEE Transactions on Circuits and Systems for Video Technology*, vol. 16, no. 3, pp. 354–362, 2006.

[19] H. Nyeem, W. Boles, and C. Boyd, "On the robustness and security of digital image watermarking," in *Proc. ICIEV 2012, IEEE*. IEEE, 2012, pp. 1136–1141.

[20] L. G. Roberts, "Machine perception of three-dimensional solids," Ph.D. dissertation, Massachusetts Institute of Technology, 1963.

[21] J. Canny, "A computational approach to edge detection," *IEEE Transactions on pattern analysis and machine intelligence*, no. 6, pp. 679–698, 1986.

[22] J. M. Prewitt, "Object enhancement and extraction," *Picture processing and Psychopictorics*, vol. 10, no. 1, pp. 15–19, 1970.

[23] N. Otsu, "A threshold selection method from gray-level histograms," *IEEE transactions on systems, man, and cybernetics*, vol. 9, no. 1, pp. 62–66, 1979.

[24] N. Dhanachandra, K. Manglem, and Y. J. Chanu, "Image segmentation using k-means clustering algorithm and subtractive clustering algorithm," *Procedia Computer Science*, vol. 54, pp. 764–771, 2015.

[25] B. Yang, D. Xiang, F. Yu, and X. Chen, "Lung tumor segmentation based on multi-scale template matching and region growing," in *Medical Imaging 2018: Biomedical Applications in Molecular, Structural, and Functional Imaging*, vol. 10578. International Society for Optics and Photonics, 2018, p. 105782Q.

[26] F. Akram, J. H. Kim, H. U. Lim, and K. N. Choi, "Segmentation of intensity inhomogeneous brain mr images using active contours," *Computational and Mathematical Methods in Medicine*, vol. 2014, 2014.

[27] M. Kass, A. Witkin, and D. Terzopoulos, "Snakes: Active contour models," *International journal of computer vision*, vol. 1, no. 4, pp. 321–331, 1988.

[28] V. Caselles, R. Kimmel, and G. Sapiro, "Geodesic active contours," *International journal of computer vision*, vol. 22, no. 1, pp. 61–79, 1997.

[29] T. F. Chan and L. A. Vese, "Active contour without edges," *IEEE Transactions on Image Processing*, no. 2, pp. 266–277, 2001.

[30] R. Maini and H. Aggarwal, "Study and comparison of various image edge detection techniques," *International journal of image processing (IJIP)*, vol. 3, no. 1, pp. 1–11, 2009.

[31] C. Li, C.-Y. Kao, J. C. Gore, and Z. Ding, "Minimization of region-scalable fitting energy for image segmentation," *IEEE transactions on image processing: a publication of the IEEE Signal Processing Society*, vol. 17, no. 10, p. 1940, 2008.

[32] L. D. Cohen and I. Cohen, "Finite-element methods for active contour models and balloons for 2-d and 3-d images," *IEEE Transactions on Pattern Analysis & Machine Intelligence*, vol. 15, no. 11, pp. 1131–1147, 1993.

[33] D. Cremers, M. Rousson, and R. Deriche, "A review of statistical approaches to level set segmentation: integrating color, texture, motion and shape," *International journal of computer vision*, vol. 72, no. 2, pp. 195–215, 2007.

[34] V. Caselles, F. Catté, T. Coll, and F. Dibos, "A geometric model for active contours in image processing," *Numerische mathematik*, vol. 66, no. 1, pp. 1–31, 1993.

[35] R. Malladi, J. A. Sethian, and B. C. Vemuri, "Topology-independent shape modeling scheme," in *Geometric Methods in Computer Vision II*, vol. 2031. International Society for Optics and Photonics, 1993, pp. 246–258.

[36] K. Zhang, H. Song, and L. Zhang, "Active contours driven by local image fitting energy," *Pattern recognition*, vol. 43, no. 4, pp. 1199–1206, 2010.

[37] L. Wang, Y. Chang, H. Wang, Z. Wu, J. Pu, and X. Yang, "An active contour model based on local fitted images for image segmentation," *Information sciences*, vol. 418, pp. 61–73, 2017.

[38] K. Ding, L. Xiao, and G. Weng, "Active contours driven by local pre-fitting energy for fast image segmentation," *Pattern Recognition Letters*, vol. 104, pp. 29–36, 2018.

[39] L. Wang, L. Zhang, X. Yang, P. Yi, and H. Chen, "Level set based segmentation using local fitted images and inhomogeneity entropy," *Signal Processing*, vol. 167, p. 107297, 2019.

[40] A. Fylakis, A. Keskinarkaus, V. Kiviniemi, and T. Seppanen, "Reversible blind data hiding for verifying integrity and authenticating mri and x-ray images," in *Proc. 9th ISMICT*. IEEE, 2015, pp. 185–189.

[41] D. Biswas, P. Das, P. Maji, N. Dey, A. Das, and S. S. Chaudhuri, "Visible watermarking within the region of non-interest of medical images based on fuzzy c-means and harris corner detection," *Computer Science & Information Technology*, pp. 161–168, 2013.

[42] K. Navas, S. A. Thampy, and M. Sasikumar, "Epr hiding in medical images for telemedicine," *International Journal of Biomedical Sciences*, vol. 3, no. 1, pp. 44–47, 2008.

[43] F. Rahimi, H. Rabbani *et al.*, "A dual adaptive watermarking scheme in contourlet domain for dicom images," *Biomedical Engineering Online*, vol. 10, no. 1, pp. 1–18, 2011.

[44] N. A. Memon, S. Gilani, and S. Qayoom, "Multiple watermarking of medical images for content authentication and recovery," in *Proc. 13th IEEE INMIC*. IEEE, 2009, pp. 1–6.

[45] H. Al-Dmour and A. Al-Ani, "Quality optimized medical image information hiding algorithm that employs edge detection and data coding," *Computer Methods and Programs in Biomedicine*, vol. 127, pp. 24–43, 2016.

[46] N. Solanki, S. K. Malik, and S. Chhikara, "Roni medical image watermarking using dwt and rsa," *International Journal of Computer Applications*, vol. 96, no. 9, pp. 30–35, 2014.

[47] P. Thiyagarajan and G. Aghila, "Reversible dynamic secure steganography for medical image using graph coloring," *Health Policy and Technology*, vol. 2, no. 3, pp. 151–161, 2013.

[48] H. Al-Dmour, A. Al-Ani, and H. Nguyen, "An efficient steganography method for hiding patient confidential information," in *2014 36th Annual International Conference of the IEEE Engineering in Medicine and Biology Society*. IEEE, 2014, pp. 222–225.

[49] W. S. Rasband, "Imagej, us national institutes of health, bethesda, maryland, usa," *http://imagej. nih. gov/ij/*, 2011.

[50] C. Rosenberger, S. Chabrier, H. Laurent, and B. Emile, "Unsupervised and supervised image segmentation evaluation," in *Advances in image and video segmentation*. IGI Global, 2006, pp. 365–393.

APPENDIX A
MATLAB CODES

A.1 Image Segmentation with the Proposed WREP Model

```
%%%%%%%%%%%%%%%%%%%%%%%%%%%%%% Segmentation Process ...
    %%%%%%%%%%%%%%%%%%%%%%%%%%%%%%
clc; clear all; close all;
Img = imread('x-ray-knee1.bmp');
Img = double(Img(:,:,1));
% -----set initial contour-----
c0 = 2;
initialLSF = ones(size(Img(:,:,1))).*c0;
initialLSF(80:100,100:120)=-c0;
uf=initialLSF;
u = initialLSF;

% -----set parameters-----
mu =1;
nu = .01*255*255;
lambda1 =1;
lambda2 =.005;
epsilon = 6.0;
timestep =0.005;
iterNum =400;
sigma =8;

% --- Local pre-fitting functions ---
K=fspecial('gaussian',round(2*sigma)*2+1,sigma);
[f1,f2,Im]=LPF(Img,K);
% -----start level set evolution-----
h2=figure(2);

for n=1:iterNum
    u = def_ACM_sKLPF(u,nu,timestep,mu,epsilon,lambda1,lambda2,f1,f2,Img);
    if mod(n,20)==0
        imagesc(Img, [0, 255]);colormap(gray);hold on;axis off,axis equal
        contour(u,[0 0],'r'); title([num2str(n), ' iterations ']);
        hold off;pause(.01);
    end
end
toc

% -----display result-----
imagesc(Img, [0, 255]);colormap(gray);hold on;axis off,axis equal
[c,h] = contour(u,[0 0],'r');
contour(uf, [0 0], 'g');
gg=imbinarize(1-u);
```

```
43
44 %%%%%%%%%%%%%%%%%%%%%%%%%%%%%%%% Decimation Process %%%%%%%%%%%%%%%%%%%%%%%%%%%%%%%%
45 BW2 = bwareafilt(gg,3);
46 CC=bwboundaries(BW2);
47 Blob1=CC{1};
48
49 xx=Blob1(:,1);
50 yy=Blob1(:,2);
51 Iconv = (roipoly(Img, yy, xx));
52 Iroi = Iconv.*Img;
53 Iroi=uint8(Iroi);
54
55 % Visualize the binary image and the contour
56 hf=figure('color','w');
57 set(hf,'units','normalized')
58 set(hf,'position',[0.1 0.1 0.8 0.6])
59 h1=subplot(1,3,1); hold on
60 imshow(Iconv)
61 plot(Blob1(:,2),Blob1(:,1),'.-g'),axis equal
62 grid on
63 axis('tight')
64
65 XLim=get(h1,'XLim'); YLim=get(h1,'YLim');
66
67 h1=get(h1,'Title');
68 msg=sprintf('Original: %u verts',size(Blob1,1));
69 set(h1,'String',msg,'FontWeight','bold','FontSize',16);
70 drawnow
71
72 % Simplify
73 fprintf('Decimate by a factor of 5\n')
74 C1=DecimatePoly(Blob1,[0.2 2]); %for knee .067
75 fprintf('Decimate by a factor of 10\n')
76 C2=DecimatePoly(Blob1,[0.1 2]); %.05 for knee
77
78 % Show the results
79 h2=subplot(1,3,2);
80 plot(C1(:,2),C1(:,1),'.-b'), axis equal
81 set(h2,'Ydir','reverse','XLim',XLim,'YLim',YLim)
82 h2=get(h2,'Title');
83 msg=sprintf('Decimated by x5: %u verts',size(C1,1)-1);
84 set(h2,'String',msg,'FontWeight','bold','FontSize',16);
85 drawnow
86
87 h3=subplot(1,3,3);
88 plot(C2(:,2),C2(:,1),'.-r'), axis equal
89 set(h3,'Ydir','reverse','XLim',XLim,'YLim',YLim)
90 h3=get(h3,'Title');
91 msg=sprintf('Decimated by x10: %u verts',size(C2,1)-1);
92 set(h3,'String',msg,'FontWeight','bold','FontSize',16);
93 drawnow
```

A.2 Level-set Function of the Proposed WREP: $def\_ACM\_sKLPF\,(\cdot)$

```
function u= def_ACM_sKLPF(u,nu,timestep,mu,epsilon,lambda1,lambda2,f1,f2,Img)
    u=NeumannBoundCond(u);
    K=curvature_central(u);
    DrcU=(epsilon/pi)./(epsilon^2.+u.^2);
    H=0.5*(1+(2/pi)*atan(u./epsilon));
    ILFI=(( f1.*H +f2.*(1 - H)));
    ISFI=(( (f1.^2).*H + (f2.^2).*(1 - H)));
    dataForce2=(f1.^2-f2.^2).*(((Img.^2)./(ISFI+eps))...
                -1-(log((ISFI+eps)./((Img.^2)+eps))));
    dataForce1=(f1-f2).*(((Img+eps)./(ILFI+eps))...
                -1-log((ILFI+eps)./(Img+eps)));
    NH=ones(3);
    dataForce=(stdfilt(Img,NH)).*((lambda1.*dataForce1)...
                +(lambda2.*dataForce2)).*(DrcU);
    PenaltyTerm=mu*(4*del2(u)-K);
    LengthTerm=nu.*DrcU.*K;
    u=u+timestep*(LengthTerm+PenaltyTerm+dataForce);
end
```

A.2.1 $NeumannBoundCond\,(\cdot)$

```
function g = NeumannBoundCond(f)
    % Neumann boundary condition
    [nrow,ncol] = size(f);
    g = f;
    g([1 nrow],[1 ncol]) = g([3 nrow-2],[3 ncol-2]);
    g([1 nrow],2:end-1) = g([3 nrow-2],2:end-1);
    g(2:end-1,[1 ncol]) = g(2:end-1,[3 ncol-2]);
end
```

A.2.2 $curvature\_central\,(\cdot)$

```
function k = curvature_central(u)
    % compute curvature
    [ux,uy] = gradient(u);
    normDu = sqrt(ux.^2+uy.^2+1e-10);
    Nx = ux./normDu;
    Ny = uy./normDu;
    [nxx,~] = gradient(Nx);
    [~,nyy] = gradient(Ny);
k = nxx+nyy;
end
```

A.3 *DecimatePoly*(·)

```
function [C_out,i_rem,CI]=DecimatePoly(C,opt,vis)
    % Check input args
    if nargin<2
        opt={};
    end

    if nargin<3 || isempty(vis)
        vis=true;
    end

    opt=CheckInputArgs(C,opt,vis);
    N=size(C,1);
    i_rem=false(N,1);
    if N≤4,
            C_out=C;
            return
    end

    % Tolerance parameter, perimeter and area of the input contour
    [Po,Emin]=PolyPerim(C);
    B_tol=Emin/2;
    Ao=PolyArea(C);
    No=N-1;

    if ¬isempty(opt)
        B_tol=opt(1);
    end

    if isempty(opt)
        opt=[B_tol 1];
    end

    Nmin=3;
    if opt(2)==2
            Nmin=round((N-1)*opt(1));
            if (N-1)==Nmin, return; end
            if Nmin<3, Nmin=3; end
    end

    % Remove (repeating) end-point
    C(end,:)=[];
    N=N-1;

    % Compute distance offset errors -------------
    D31=circshift(C,[-1 0])-circshift(C,[1 0]);
    D21=C-circshift(C,[1 0]);
    dE_new2=sum(D31.^2,2);

```

```
49      % Find closest points to current vertices on the new edges
50      t=sum(D21.*D31,2)./dE_new2;
51      t(t<0)=0;
52      t(t>1)=1;
53      V=circshift(C,[1 0])+bsxfun(@times,t,D31);
54
55      % Evaluate distance^2
56      Err_D2=sum((V-C).^2,2);
57
58      % Initialize distance error accumulation array
59      DEAA=zeros(N,1);
60
61      % Begin decimation -----------------------
62      idx_ret=1:N; % keep track of retained vertices
63
64      while true
65              % Find vertices whose removal will satisfy the decimation criterion
66              idx_i=Err_D2<B_tol;
67              if sum(idx_i)==0 && N>Nmin && opt(2)==2
68                      B_tol=B_tol*sqrt(1.5);
69                      continue
70              end
71
72              idx_i=find(idx_i); %find non zero elements
73              if isempty(idx_i) || N==Nmin, break; end
74              N=N-1;
75
76              % Vertex with the smallest net error
77              [¬,i_min]=min(Err_D2(idx_i));
78              idx_i=idx_i(i_min);
79
80              % Update distance error accumulation array
81              DEAA(idx_i)=DEAA(idx_i)+sqrt(Err_D2(idx_i));
82              i1=idx_i-1; if i1<1, i1=N; end
83              i3=idx_i+1; if i3>N, i3=1; end
84              DEAA(i1)=DEAA(idx_i);
85              DEAA(i3)=DEAA(idx_i);
86
87              % Recompute errors of vertices adjacent to vertex marked for deletion
88              i1_1=i1-1; if i1_1<1, i1_1=N; end
89              i1_3=i3;
90              i3_1=i1;
91              i3_3=i3+1; if i3_3>N, i3_3=1; end
92
93              err_D1=RecomputeErrors(C([i1_1,i1,i1_3],:));
94              err_D3=RecomputeErrors(C([i3_1,i3,i3_3],:));
95
96              % Update errors
97              Err_D2(i1)=(sqrt(err_D1)+ DEAA(i1)).^2;
98              Err_D2(i3)=(sqrt(err_D3)+ DEAA(i3)).^2;
99
```

```
100             % Remove vertex
101             C(idx_i,:)=[];
102             idx_ret(idx_i)=[];
103             DEAA(idx_i)=[];
104             Err_D2(idx_i)=[];
105     end
106
107     C=[C;C(1,:)]; C_out=C;
108     i_rem(idx_ret)=true;
109     i_rem=¬i_rem;
110     i_rem(end)=i_rem(1);
111
112     % Perimeter and area of simplified contour
113     P=PolyPerim(C);
114     A=PolyArea(C);
115
116     % Contour info
117     CI.in.num_verts=No;
118     CI.in.perimeter=Po;
119     CI.in.area=Ao;
120     CI.out.num_verts=N;
121     CI.out.perimeter=P;
122     CI.out.area=A;
123     % Effect of decimation on total area and perimeter of the contour
124     if ¬vis, return; end
125     fprintf('%+20s%+15s%+11s\n','# of verts','perimeter','area')
126     fprintf('-----------------------------------------------------\n')
127     fprintf('%-10s%-16u%-16.3f%-16.3f\n','in',No,Po,Ao)
128     fprintf('%-10s%-16u%-16.3f%-16.3f\n','out',N,P,A)
129     fprintf('-----------------------------------------------------\n')
130     fprintf('%-10s%-16.3f%-16.3f%-16.3f\n','% ...
            change',(N-No)/No*100,(P-Po)/Po*100,(A-Ao)/Ao*100)
131 end
132
133 %=========================================================================
134 function err_D2=RecomputeErrors(V)
135     D31=V(3,:)-V(1,:);
136     D21=V(2,:)-V(1,:);
137     dE_new2=sum(D31.^2,2); % length^2 of potential new edge
138     % Find closest point to the current vertex on the new edge
139     t=sum(D21.*D31,2)/dE_new2;
140     t(t<0)=0;
141     t(t>1)=1;
142     p=V(1,:)+bsxfun(@times,t,D31);
143     % Evaluate the distance^2
144     err_D2=sum((p-V(2,:)).^2);
145 end
146
147 %=========================================================
148 function A=PolyArea(C)
149     % Polygon area
```

```
150     dx=C(1:(end-1),1)-C(2:end,1);
151     dy=C(2:end,2)+C(1:(end-1),2);
152     A=sum(dx.*dy)/2;
153     A=abs(A);
154 end
155 
156 %=======================================================
157 function [P,Emin]=PolyPerim(C)
158     % Polygon perimeter
159     dE=C(2:end,:)-C(1:(end-1),:);
160     dE=sqrt(sum(dE.^2,2));
161     P=sum(dE);
162     Emin=min(dE);
163 end
164 
165 %=======================================================
166 function opt=CheckInputArgs(C,opt,vis)
167 % Check validity of the input arguments
168 siz=size(C);
169     if numel(siz)~=2 || siz(2)>siz(1) || ~isnumeric(C) || ~ismatrix(C) || ~...
            ismatrix(C)
170         error('1st input argument (C) must be a N-by-2 array')
171     end
172     if norm(C(1,:)-C(end,:))>1E-6
173         error('First and last points in C must be the same')
174     end
175     if isempty(opt)
176         return;
177     end
178     if ~isnumeric(opt) || numel(opt)~=2
179         error('Invalid entry for 2nd input argument (opt)')
180     end
181     if ~(opt(2)==1 || opt(2)==2)
182         error('Invalid entry for 2nd input argument (opt). opt(2) must be set ...
                to 1 or 2.')
183     end
184     if opt(2)==1 && opt(1)≤eps
185         error('Invalid entry for 2nd input argument (opt). When opt(2)==1, ...
                opt(1) must be greater than zero.')
186     end
187     if opt(2)==2 && (opt(1)≤eps || opt(1)≥1)
188         error('Invalid entry for 2nd input argument (opt). When opt(2)==2, ...
                opt(1) must be on the interval (0,1).')
189     end
190     if numel(vis)~=1 || ~islogical(vis)
191         error('Invalid entry for 3rd input argument (vis). vis must be binary.')
192     end
193 end
```

APPENDIX B
Additional Settings and Results

B.1 Constants Used for LHIF and LPF Models

Table B.1: Constant Parameters Used for LHIF Model

Test Image (LHIF)	σ	ν	λ_1	λ_2	μ	ε	Δt
MRI-brain21	25	.01*255*255	1	0.8	2	5	0.01
DSA-angiogram10	20	.03*255*255	1	0.4	2	5	0.01
Mammogram	5	.03*255*255	1	0.5	2	5	0.01
US-urogenital1	7	.04*255*255	1	0.5	2	7	0.05
MRI-left-ventricle	11	.1*255*255	1	0.4	2	5	0.01
MRI-nonuniform	20	.03*255*255	1	0.6	2	5	0.01
CT-cardiac	15	.01*255*255	1	0.5	2	6	0.05
MR-brain	15	.01*255*255	1	0.2	2	5	0.01
Fluorescence-micrograph	30	.02*255*255	1	0.05	2	5	0.05
CT-knee1	35	.04*255*255	1	0.05	2	6	0.01
CT-kidney3	10	.004*255*255	1	0.05	2	5	0.05
CT-kidney7	20	.04*255*255	1	0.1	2	5	0.05
CT-chest1	15	.002*255*255	1	0.005	2	5	0.01
X-ray-knee2	25	.01*255*255	1	0.1	2	5	0.005
X-ray-leg1	15	.006*255*255	1	0.05	2	5	0.01
Fluoroscopy-bladder2	15	.009*255*255	1	0.03	2	5	0.01
fluoroscopy-gastrointestinal5	25	.04*255*255	1	0.05	2	5	0.01
DSA-angiogram9	5	.008*255*255	1	0.2	2	5	0.05
MRI-brain38	8	.007*255*255	1	0.03	2	7	0.04
MRI-brain39	20	.01*255*255	1	0.05	2	7	0.01
X-ray-knee1	10	.001*255*255	1	0.05	2	5	0.1
Fluoroscopy-neck3	8	.07*255*255	1	0.8	2	5	0.005
Car	7	.008*255*255	1	0.05	2	5	0.05
CT-heart	20	.007*255*255	1	0.1	2	5	0.05
F95	10	.0007*255*255	1	0.3	2	5	0.05
Blood vessel angiography	6	.002*255*255	1	0.5	2	3	0.05
Shapes-nonuniform	8	.002*255*255	1	0.2	2	3	0.1
Shape-inhomogeneous	15	.002*255*255	1	0.1	2	3	0.01
Star5	10	.0003*255*255	1	0.8	1	5	0.1
T-shape	18	.08*255*255	1	0.15	1	5	0.005
Vessel1	8	.001*255*255	1	0.15	2	2	0.1
Vessel2	7	.001*255*255	1	0.15	2	2	0.1
MRI-brain	6	.002*255*255	1	0.15	2	5	0.01

Table B.2: Constant Parameters Used for LPF Model

Test Image (LPF)	σ	ν	λ_1	λ_2	μ	ε	Δt
MRI-brain21.bmp	10	.01*255*255	1	1	2	1	0.01
DSA-angiogram10.bmp	6	.004*255*255	1	1	2	1	0.01
Mammogram	1	.04*255*255	1	1	2	1	0.01
US-urogenital1	2	.1*255*255	1	1	2	1	0.01
MRI-left-ventricle	15	.05*255*255	1	1	2	1	0.01
MRI-nonuniform	5	.05*255*255	1	1	2	1	0.01
CT-cardiac	12	.04*255*255	1	1	2	1	0.01
MR-brain	6	.05*255*255	1	1	2	1	0.01
Fluorescence-micrograph	15	.1*255*255	1	1	2	1	0.01
CT-knee1	10	.5*255*255	1	1	2	1	0.01
CT-kidney3	12	.02*255*255	1	1	2	1	0.01
CT-kidney7	10	.02*255*255	1	1	2	1	0.01
CT-chest1	10	.02*255*255	1	1	2	1	0.01
X-ray-knee2	10	.01*255*255	1	1	2	1	0.01
X-ray-leg1	4	.001*255*255	1	1	2	1	0.01
Fluoroscopy-bladder2	2	.4*255*255	1	1	2	1	0.01
Fluoroscopy-gastrointestinal5	3	.01*255*255	1	1	2	1	0.01
DSA-angiogram9	10	.01*255*255	1	1	2	1	0.01
MRI-brain38	8	.06*255*255	1	1	2	1	0.01
MRI-brain39	12	.1*255*255	1	1	2	1	0.01
X-ray-knee1	12	.2*255*255	1	1	2	1	0.01
Fluoroscopy-neck3	1	.04*255*255	1	1	2	1	0.05
Car	5	.1*255*255	1	1	1	1	0.02
Heart_ct	4	.04*255*255	1	1	1	1	0.01
F95	3	.0008*255*255	1	1	1	1	0.05
Lathi	3	02*255*255	1	1	1	1	0.1
Shapes-nonuniform	2	.02*255*255	1	1	1	1	0.1
Shape-inhomogeneous	2	.02*255*255	1	1	2	1	0.01
Star5	2	.0003*255*255	2	1	2	1	0.01
T-shape	4	.04*255*255	1	1	2	1	0.05
Vessel1	3	.01*255*255	1	1	2	1	0.1
Vessel2	4	.006*255*255	1	1	2	1	0.01
MRI-brain	2	.05*255*255	1	1	2	1	0.01

B.2 RoI Segmentation Performance

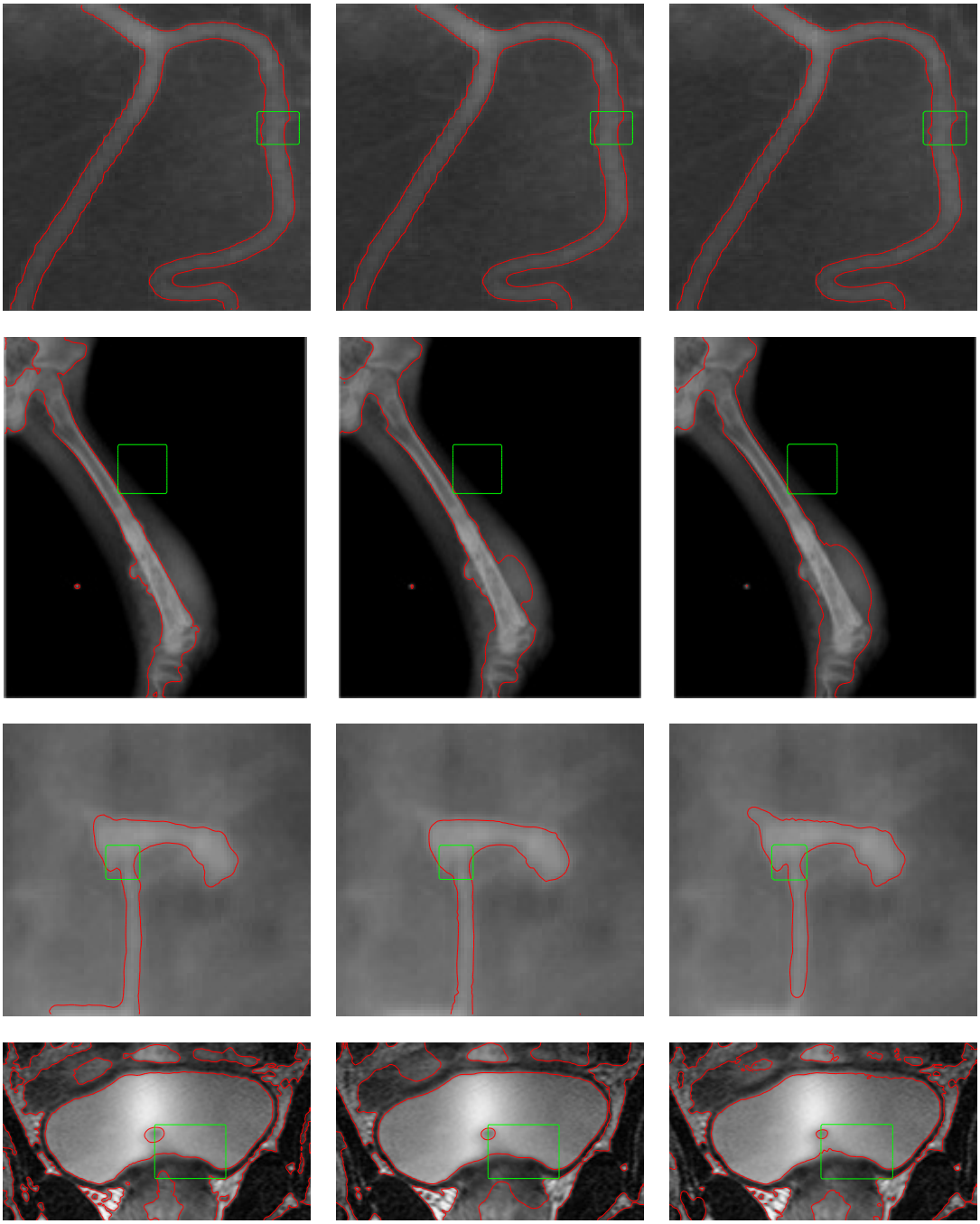

Figure B.1: Segmentation results for the intensity-inhomogeneous images (from top, internal blood vessel images, X-ray of knee and MR image) of the schemes: proposed (*left column*), LPF [38] (*middle column*), and LHIF [37] (*right column*).

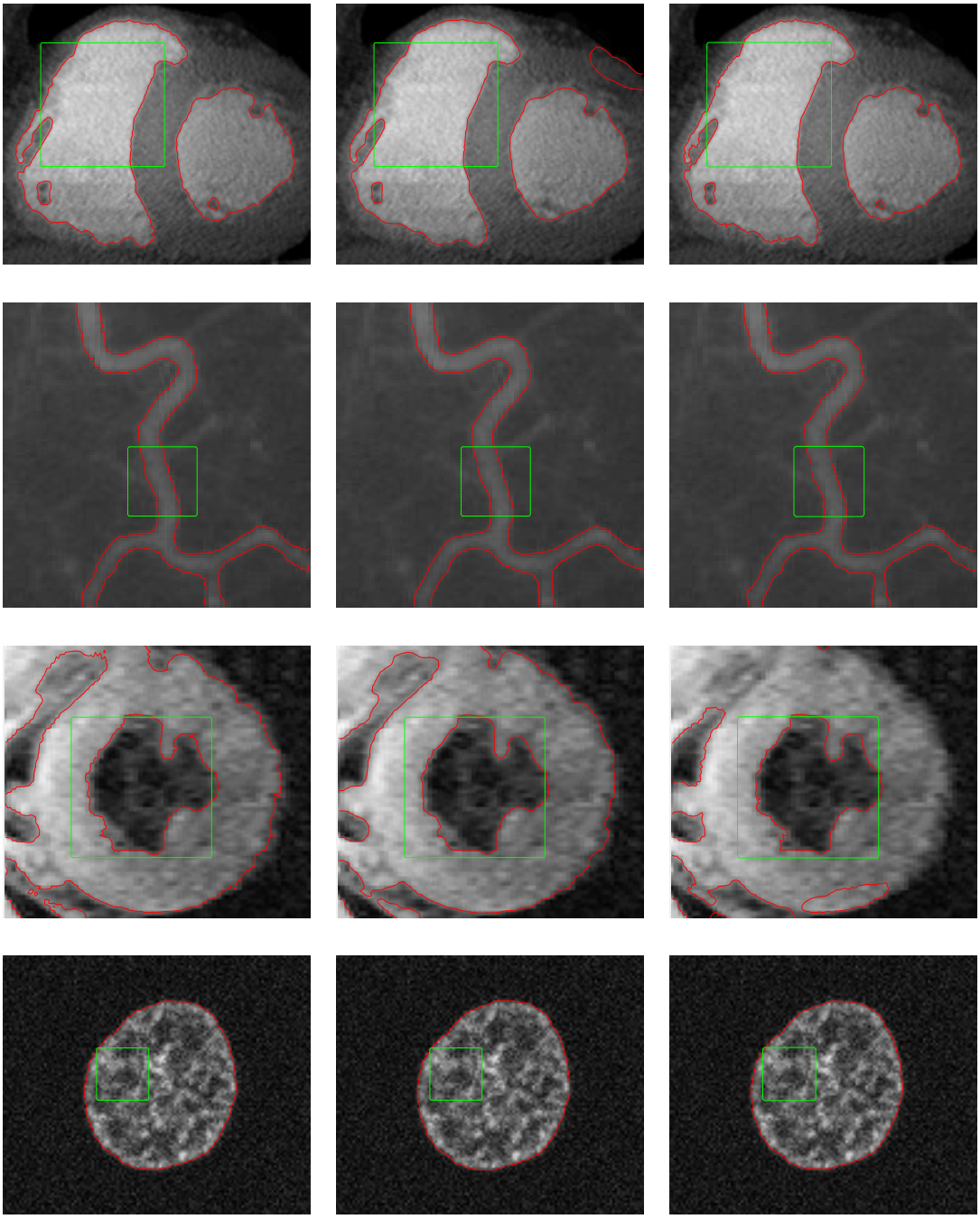

Figure B.2: Segmentation results for the noisy images (from top, CT heart and vessel, MRI of left ventricle and Fluorescence micrograph of nucleus) of the schemes: proposed (*left column*), LPF [38] (*middle column*), and LHIF [37] (*right column*).

B.3 RoI Representation Performance

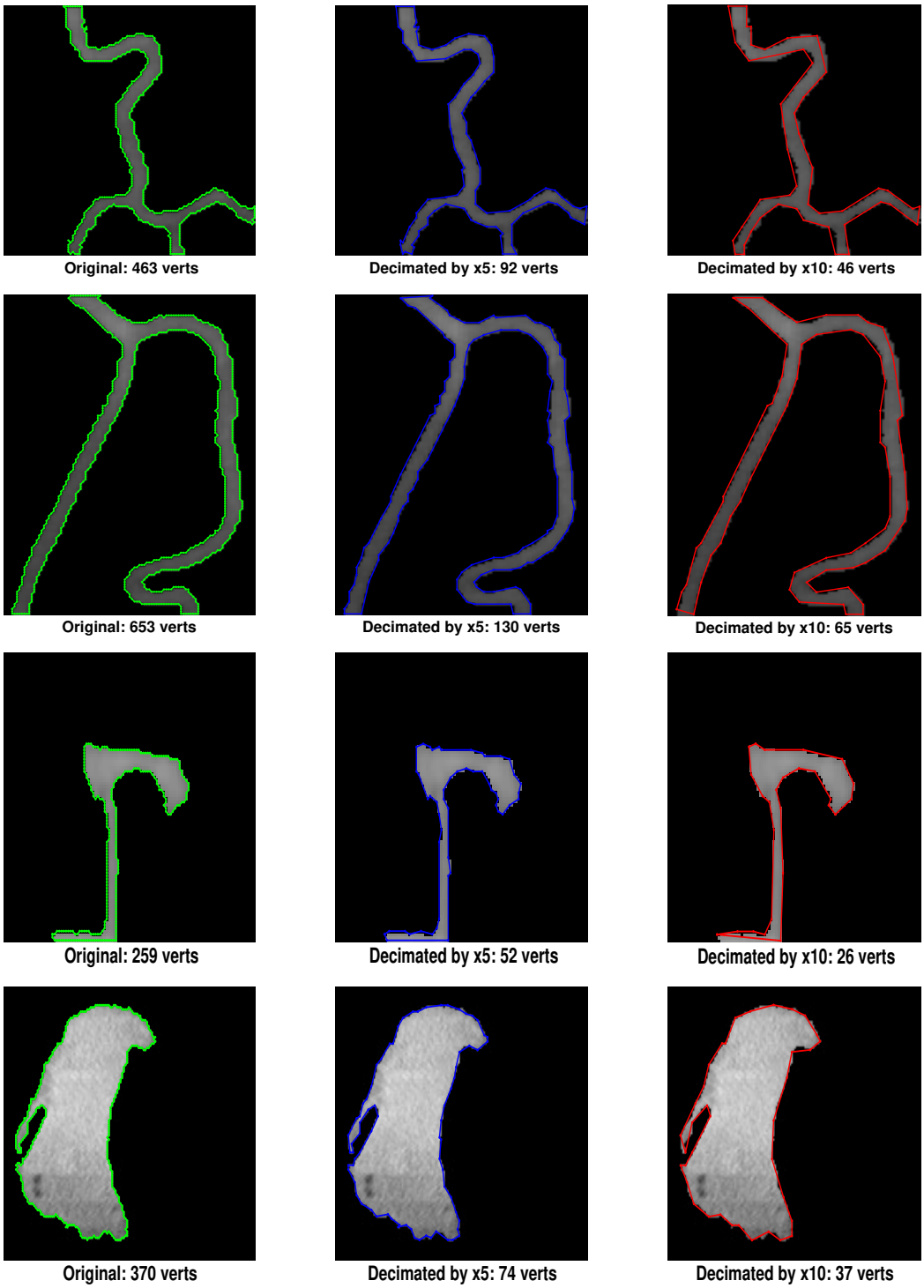

Figure B.3: Vertex number decimation of segmented RoI in various MIs: original RoI (*left column*), RoI with 5 times decimation (*middle column*), and RoI with 10 times decimation (*right column*).

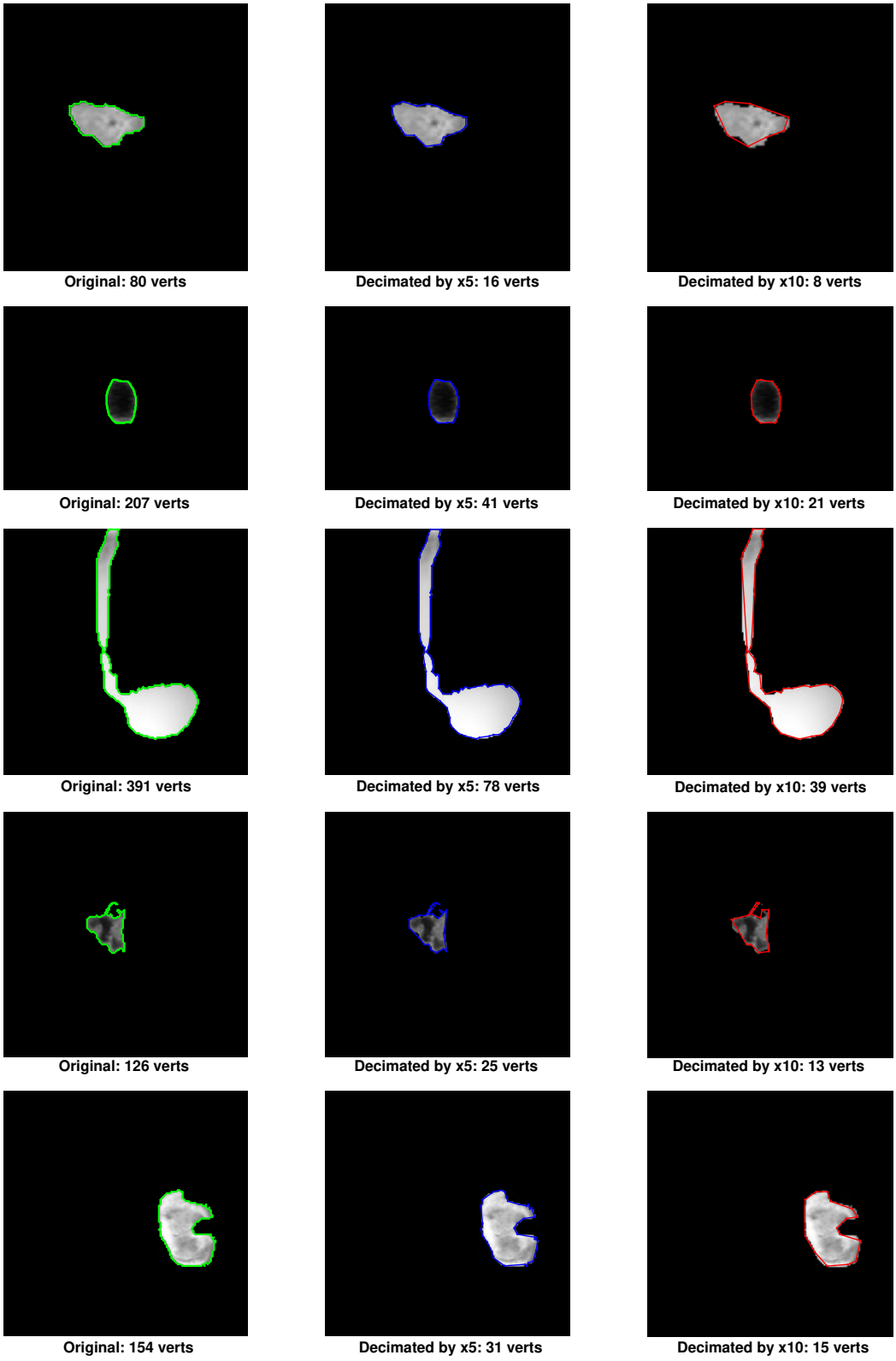

Figure B.4: Vertex number decimation of segmented RoI in various MIs: original RoI (*left column*), RoI with 5 times decimation (*middle column*), and RoI with 10 times decimation (*right column*).